ELSEVIER

Mercury: Radar images of the equatorial and midlatitude zones

John K. Harmon [a,*], Martin A. Slade [b], Bryan J. Butler [c], James W. Head III [d],
Melissa S. Rice [a], Donald B. Campbell [e]

[a] *National Astronomy and Ionosphere Center, Arecibo Observatory, HC3 Box 53995, Arecibo, PR 00612, USA*
[b] *Jet Propulsion Laboratory, California Institute of Technology, Pasadena, CA 91109, USA*
[c] *National Radio Astronomy Observatory, Socorro, NM 87801, USA*
[d] *Department of Geological Sciences, Brown University, Providence, RI 02912, USA*
[e] *Department of Astronomy, Cornell University, Ithaca, NY 14853, USA*

Abstract

Radar imaging results for Mercury's non-polar regions are presented. The dual-polarization, delay-Doppler images were obtained from several years of observations with the upgraded Arecibo S-band (λ12.6-cm) radar telescope. The images are dominated by radar-bright features associated with fresh impact craters. As was found from earlier Goldstone-VLA and pre-upgrade Arecibo imaging, three of the most prominent crater features are located in the Mariner-unimaged hemisphere. These are: "A," an 85-km-diameter crater (348° W, 34° S) whose radar ray system may be the most spectacular in the Solar System; "B," a 95-km-diameter crater (343° W, 58° N) with a very bright halo but less distinct ray system; and "C," an irregular feature with bright ejecta and rays distributed asymmetrically about a 125-km source crater (246° W, 11° N). Due south of "C" lies a "ghost" feature (242° W, 27° S) that resembles "A" but is much fainter. An even fainter such feature is associated with Bartok Crater. These may be two of the best mercurian examples of large ejecta/ray systems observed in an intermediate state of degradation. Virtually all of the bright rayed craters in the Mariner 10 images show radar rays and/or bright rim rings, with radar rays being less common than optical rays. Radar-bright craters are particularly common in the H-7 quadrangle. Some diffuse radar albedo variations are seen that have no obvious association with impact ejecta. In particular, some smooth plains regions such as the circum-Caloris plains in Tir, Budh, and Sobkou Planitiae and the interiors of Tolstoj and "Skinakas" basins show high depolarized brightness relative to their surroundings, which is the reverse of the mare/highlands contrast seen in lunar radar images. Caloris Basin, on the other hand, appears dark and featureless in the images.
© 2006 Elsevier Inc. All rights reserved.

Keywords: Mercury; Mercury, surface; Radar observations

1. Introduction

A major upgrade to the Arecibo telescope, completed in late 1997, substantially enhanced the sensitivity of the S-band planetary radar. Among the opportunities this afforded was the ability to make higher quality radar images of Mercury. An obvious first objective was to make improved high-resolution images of the planet's putative polar ice features. Successful imaging observations of the north pole were conducted in 1998–1999, and the results were published in Harmon et al. (2001). At the same time, we were also interested in doing a radar imaging sur-

vey covering the entire planet. The objective was to image the hemisphere left unimaged by Mariner 10 as well as to obtain radar images over the Mariner-imaged hemisphere that could be compared with the optical images. This was necessarily a longer-term project, requiring making observations near inferior conjunction over a period of several years and spanning a range of Mercury sub-Earth longitudes and latitudes. Although in the course of this project we have obtained some new polar images, we will defer reporting on these to a later paper. Our purpose here is to report the results of our post-upgrade Arecibo radar imaging survey of Mercury's equatorial and midlatitude regions.

Little Mercury radar imaging work had been done prior to the 1990s, and there was certainly nothing to compare with the

* Corresponding author. Fax: +1 787 878 1861.
  E-mail address: harmon@naic.edu (J.K. Harmon).

extensive radar results achieved for the Moon and Venus (e.g., Zisk et al., 1974; Campbell and Burns, 1980). This was due, in part, to the difficulties presented by the relatively weak Mercury echoes, although a lower level of intrinsic interest in the planet no doubt also contributed. The first delay-Doppler radar images of Mercury were obtained with the Goldstone S-band radar over three decades ago (Zohar and Goldstein, 1974), and several additional Goldstone images were published in the following decade (Clark et al., 1988). An extensive program of delay-Doppler observations was carried out at Arecibo during 1978–1984 (Harmon et al., 1986; Harmon and Campbell, 1988), but these were used mainly for constructing topographic profiles along Mercury's Doppler equator and produced no published images. All of the early Mercury imaging exploited the specular component of the polarized echo and thus concentrated on imaging the zone contained within a few degrees of the sub-Earth point. Within this region, the polarized images can delineate large-scale surface relief such as crater rims and provide some semblance of the view given by an optical image. Outside this sub-Earth zone, one can still pick up high-angle specular glints as well as "diffuse component" echoes associated with high-angle backscatter off small (wavelength-scale) structure. Hence, given a radar of sufficient sensitivity, one should be able to extend coverage to the entire visible disk as well as map out spatial variations in small-scale surface roughness. The diffuse echo appears in both the polarized and depolarized polarizations (see Section 2). Depolarized images are particularly useful for mapping diffuse backscatter, since they are completely free of the specular glare that dominates the polarized echo. However, until the 1990s the only dual-polarization radar observations reported for Mercury were those of Goldstein (1970, 1971). These were CW (continuous-wave) observations, which are suitable for measuring Doppler spectra but not for imaging. Goldstein's work was interesting nonetheless, as it revealed some distinct features in the depolarized Doppler spectrum. This suggested that a full-disk radar image of the planet might show some interesting reflectivity features if one were to look with a sufficiently sensitive radar.

The first full-disk, dual-polarization images of Mercury were finally made in 1991. Slade et al. (1992) used the synthesized beam of the Very Large Array (VLA) to make radar images of the planet as illuminated by Goldstone X-band (λ3.5-cm) transmissions (see also Butler et al., 1993; Butler, 1994; Muhleman et al., 1995). This method, which had been used two years earlier to make radar images of Mars (Muhleman et al., 1991), had the great advantage of avoiding the "overspreading" and "north–south ambiguity" problems inherent in delay-Doppler. The Goldstone-VLA imaging produced the startling discovery of a very bright spot at the north pole suggestive of ice. It also showed several other prominent radar-bright features at low to middle latitudes, three of which could account for Goldstein's two main CW spectral features. That same year (1991) we began a program of dual-polarization imaging observations of Mercury with the Arecibo S-band (λ12.6-cm) radar. To mitigate echo overspreading effects on the full-disk images, we employed the same "long-code" delay-Doppler technique as that tested out the previous year on Mars. (Mercury, though a much slower rotator than Mars, is still moderately overspread, even at S band.) The Arecibo images confirmed the north polar "ice" feature, revealed a similar south polar feature, and showed some of the same major non-polar features (Harmon and Slade, 1992). Subsequently, improved Arecibo images were made from averages of many long-code runs from 1991–1992. These images had a resolution down to 15 km, which was an order of magnitude finer than for the Goldstone-VLA images. This resolution was sufficient to resolve the polar ice features and identify their host craters (Harmon et al., 1994), as well as to identify one of the "Goldstein features" as a spectacular bright-rayed impact crater (Harmon, 1997).

The Arecibo upgrade brought an order-of-magnitude improvement in the S-band system sensitivity. This has enabled us to achieve even finer Mercury image resolution while still maintaining decent image quality in terms of signal-to-noise ratio (S/N). The improved resolution has not only brought out fine detail in some of the larger known structures (such as the "Goldstein features"), but has also enabled us to resolve ejecta features around much smaller fresh craters. However, S/N remains an important limiting factor, especially at the larger planet distances and at higher incidence angles near the planet limbs. In fact, image quality is seriously degraded for most non-ice features at mercurian latitudes above 50°, which is the reason we have qualified the title with the "equatorial and midlatitude" phrase.

We begin the paper with a discussion of the radar observations and image reduction. This is followed by the heart of the paper, which presents a gallery of images on a region-by-region basis along with some brief commentary. We then conclude with a short discussion of some of the major findings. Throughout the paper, we will make comparisons with earlier Mercury results such as the Mariner 10 and Goldstone-VLA imaging as well as some more recent Earth-based telescopic imaging. We will also draw comparisons with lunar radar results in our discussions.

2. Observations and analysis

Most of the images shown in this paper are from long-code observations made during the period 2000–2005 (excluding 2003). Since a long-code capability was not available on the upgraded system until 2000, we have also used a few standard (repeating-code) observations from 1998–1999. Post-upgrade Mercury imaging observations have been made on a total of 43 dates since 1998; these dates and various observing parameters are listed in Table 1. The images shown in this paper were derived from 31 of these dates. Most of the observations were made near inferior conjunction (to minimize target distance and maximize echo strength), although a few more distant observations were also made; the range of Mercury distances was 0.56–1.13 AU. The planet coverage is shown in Fig. 1, which plots the sub-Earth points of the observations.

The observations were made with the S-band radar on the 305-m Arecibo telescope, transmitting at 2380 MHz (12.6-cm wavelength). The new dual-klystron system gave a typical transmitted power of 800–900 kW, or twice the pre-upgrade

Table 1
Observations and coverage

Longitude	Latitude	Δ (AU)	Dates	Baud (μs)	Type[a]
5–17	+4.5	0.65	1–3 Jun 2001	10	LC
18–39	−4.5	0.58	14–17 Apr 2004	10	LC
46	+9.3	0.75	17 Aug 2005	10	LC
82	+7.3	0.56	13 Jun 2001	10	LC
119	+5.0	0.56	2 Jun 2002	10	LC
135–142	+11.7	0.58	25–26 Jul 1999	10	S
163–169	+5.7	0.63	9–10 Jun 2002	10	LC
174–181	+11.2	0.63	16–17 Aug 1998	20	S
195–201	+8.8	0.73	15–16 Jul 2005	10	LC
230–235	+5.7	0.82	21–22 Jun 2002	10	LC
230–236	+7.4	0.80	7–8 Jul 2001	20	LC
241	−1.7	1.13	22 Apr 2002	10	LC
241–247	+10.3	0.69	8–9 Aug 2004	10	LC
273–278	−1.1	0.95	29–30 Apr 2002	10	LC
278–285	+11.2	0.63	14–15 Aug 2004	10	LC
309–314	−0.3	0.80	6–7 May 2002	10	LC
312	+11.4	0.62	19 Aug 2004	10	LC
328–335	+11.8	0.60	5–6 Aug 2005	10	LC
346–353	−7.5	0.64	24–25 Mar 2005	10	LC
352–358	+7.5	0.77	2–3 Jul 1999	20	S
352–10	+6.3	0.70	15–18 Jun 2000	20	LC
355	+1.0	0.66	14 May 2002	10	LC

[a] LC = long code, S = standard (repeating) code.

power. (The power was lower for the 2005 observations owing to transmitter problems.) All transmissions were circularly polarized. The transmissions were modulated with a binary phase code with a baud (phase-flip interval) of either 10 or 20 μs, with most of the long-code observations using 10 μs. The long-code observations used a $10^{40} - 1$ maximal-length shift-register code, which was effectively non-repeating during an observation. The standard-code observations used a code length of either 1023 (20 μs) or 2047 (10 μs).

All receiving was done in both (orthogonal) senses of circular polarization. Following standard practice, we will use the terms "OC" and "SC" to denote the receive polarization senses that are the opposite of, or the same as, the transmitted sense, respectively. All receive signal sampling was done at a rate of one complex sample per baud. The sampled data were analyzed to partition the echo into a delay-Doppler array, using the long-code analysis techniques discussed in Harmon (2002).

The long-code decoding was done by computing a lagged-product time series for each delay. To speed up processing, these time series were smoothed and decimated by a factor of 512 or 256 for a baud of 10 or 20 μs, respectively. This gave a Nyquist bandwidth of 195 Hz, or roughly twice Mercury's Doppler bandwidth at S band. The Doppler spectrum of the smoothed time series was then computed, using Fourier transform lengths of 8192 (10 μs) or 4096 (20 μs). This gave frequency resolutions of 0.0238 Hz (10 μs) or 0.0477 Hz (20 μs). The spectra for all the delays comprised a delay-Doppler array, which was then averaged over the full receive time of an observing "run" (or transmit/receive cycle). Examples of long-code delay-Doppler arrays are shown in Fig. 2. Also shown for comparison are standard-code delay-Doppler arrays. This shows the advantages of long-code over standard delay-Doppler, namely, the elimination of (a) the Doppler aliasing associated with target
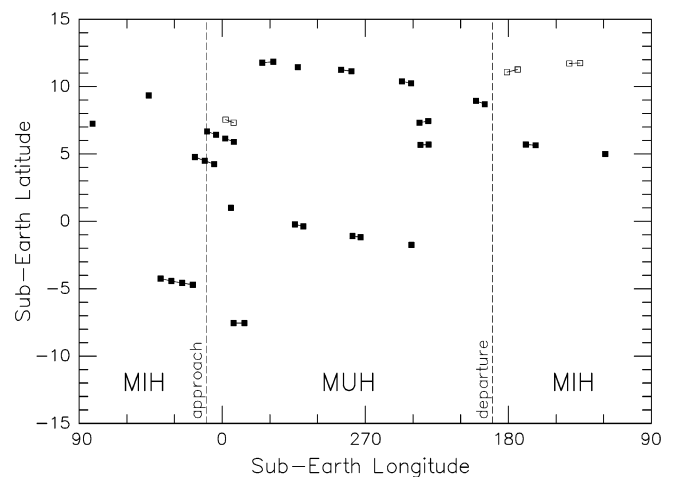

Fig. 1. Sub-Earth tracks for the post-upgrade Arecibo radar observations. Each symbol is the mean sub-Earth point for a given day's long-code (filled square) or standard-code (open square) observation. The terminators (dashed) at the Mariner 10 approach and departure phases separate the Mariner-imaged (MIH) and Mariner-unimaged (MUH) hemispheres.

overspreading, and (b) the deterministic self-clutter associated with code sidelobe leakage. The one disadvantage of long-code is the introduction of a random self-clutter that effectively increases the background noise. This clutter is negligible (<5%) for the SC polarization but can raise the OC noise level by as much as 50%. For more detailed treatment of the long-code method, and associated data analysis techniques, see Harmon et al. (1999) and Harmon (2002).

The mapping process converted the delay-Doppler arrays to planetary (latitude/longitude) coordinates. A separate map was generated for each run-averaged array. A final map was then made by adding the maps from all of the runs from between
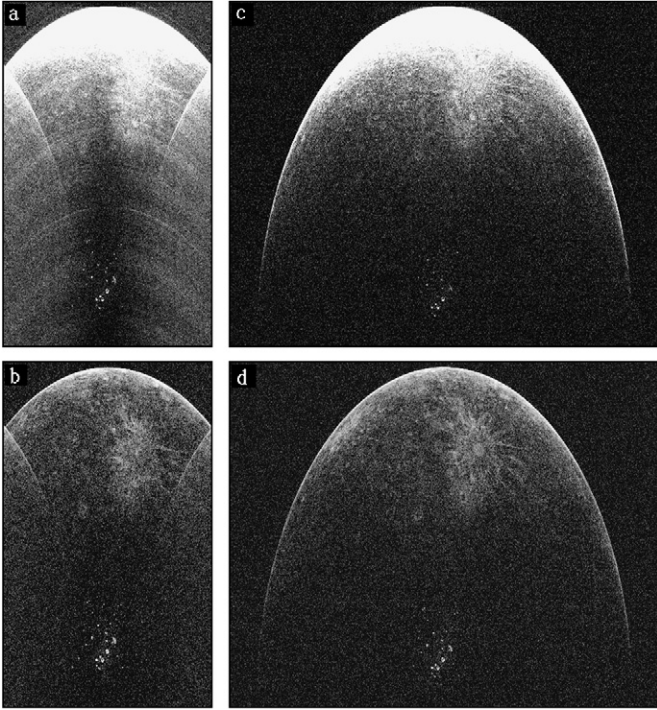
Fig. 2. Delay-Doppler arrays for Mercury illustrating the two different observing modes: (a) standard-code, OC polarization; (b) standard-code, SC polarization; (c) long-code, OC polarization; (d) long-code, SC polarization. The standard-code data are from July 3, 1999 and the long-code data are from June 16, 2000. The horizontal axis is Doppler and the vertical axis is delay. The echo's leading edge is at top, the putative north polar ice spots are at bottom center, and feature "A" is the prominent rayed feature. The gray scale is normalized to the peak polar echo brightness, so the OC specular echo at the leading edge is saturated. Note the echo folding from Doppler aliasing and OC streaking from code sidelobe leakage in the standard-code arrays. The figure is reproduced from Harmon (2002).

one and four consecutive days. The longitude smear from planet rotation during a run was ∼0.05° or ∼2 km, which was comparable with the intrinsic resolution in the Doppler coordinate. The intrinsic resolution in delay was 1.5–3 km, but the effective latitude resolution could be several times coarser due to the $\csc\theta$ incidence-angle projection and delay-Doppler tangency effects near the Doppler equator. The actual resolution of the map display was set by our standard 512×512 pixel display and the particular map dimensions; for the images in this paper, the pixel resolution was between 0.06° and 0.18° (2.5–7.5 km).

Maps were made for both OC and SC polarizations. The OC echo has a strong specular peak at small incidence angles that tails off to a broad halo associated with diffuse scatter from λ-scale roughness. To get around the dynamic range problem posed by the specular echo, we divided the single-run OC maps by a composite scattering law comprising a Hagfors quasispecular component (with an assumed C parameter of 65 and reflectivity of 0.058) and a $\cos^{3/2}\theta$ diffuse component (with an assumed diffuse OC albedo of 0.0129). We then set the maximum gray-scale level of the final multi-run OC image to ∼10–20% of the brightest pixel. This scale truncation was needed to reduce the residual OC dynamic range problem posed by specular glints off crater walls. The SC maps, which

contain only the depolarized component of the diffuse echo, are displayed in raw form without scattering-law correction or (unless otherwise noted) scale truncation.

The images suffer from the "north–south ambiguity" inherent in delay-Doppler mapping of targets whose disks (unlike the Moon's) are smaller than the telescope beam. This ambiguity appears as a folding of the images about the "Doppler equator" (the central dark belt seen running east–west in our images). For Venus it is possible, owing to the planet's relatively large apparent disk size, to mitigate N/S-ambiguity foldover by offsetting the telescope beam toward the hemisphere (N or S) of interest. We have not attempted this with our Mercury observations, owing to the planet's smaller apparent disk size and weaker echoes. Other methods for ambiguity removal based on formal algorithms have been proposed, but these are difficult to implement and inevitably introduce additional image noise. We have not attempted such a formal N/S-ambiguity removal for this paper, opting instead to use sub-Earth latitude diversity to resolve the ambiguity on a case-by-case basis. This is easily done by comparing images obtained at different sub-Earth latitudes and rejecting those features whose mapped positions change when the images are blinked. In many cases, spurious features in multiday averages can also be identified by the smearing associated with changing sub-Earth aspect. Of course, for some areas the radar feature ambiguity is also easily resolved simply by comparing with Mariner or VLA images. In this paper, the reader can assume that any features referenced explicitly by location or highlighted in a smaller-scale detail image has had its true location determined by one of these means. Nevertheless, any image will be corrupted to some extent by ambiguity foldover, even if the particular feature of interest dominates the image.

3. Regional images and radar features

In this section, we present a gallery of images taken around the planet. These include large-scale images (90° or more on a side) along with smaller-scale detail images (a few degrees or tens of degrees on a side) of particular features of interest. All images are rendered in gray scale, with lighter shades corresponding to higher radar reflectivity. The image brightness or reflectivity is normalized to a (dimensionless) "specific cross section" $\sigma°$, which is the radar cross section per unit surface area. For each SC image, we give the maximum brightness $\sigma°_{sc}(\text{max.})$ in the figure caption.

The OC images are dominated by specular reflection within about 20° of the subradar point. These OC (or "polarized") images, which resemble optical images, are best for identifying sharp surface relief such as crater rims. In the SC (or "depolarized") images, the strongest factor influencing brightness is the abundance of wavelength-scale surface roughness, with dielectric variations probably being of secondary importance. The brightness in these depolarized images appears to be dominated by rough impact ejecta, and a reasonable working assumption is that this brightness is correlated with the freshness of the impact (Thompson et al., 1981).

For clarity of presentation, we have organized our image presentation on a regional basis, beginning with those regions
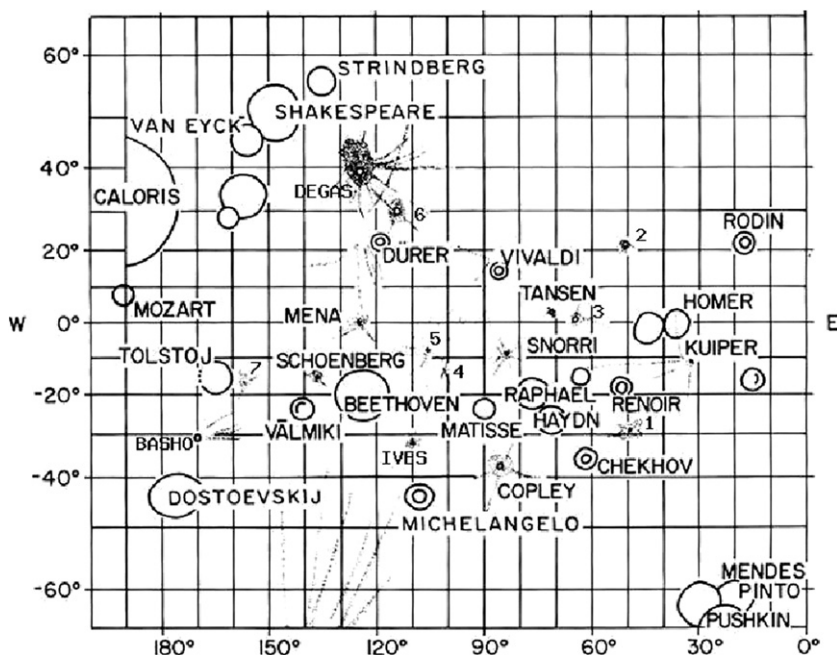
Fig. 3. Map schematic of Mercury's major basins and ray systems in the MIH. The map is adapted from Fig. 8 of the Atlas of Mercury (Davies et al., 1978). Some additional crater names have been added, along with the "MRC" numbers for the unnamed rayed craters.

showing the most dramatic SC features. Those that we dub the "Mariner-Approach Region" and "Trans-Caloris Region" roughly correspond to the two original Goldstone-VLA views in Slade et al. (1992); these contain the strongest depolarized features on the planet, which also happen to be the sources of the two CW spectral features identified by Goldstein (1970). We then discuss the "Caloris Region," which includes the planet's dominant impact basin as well as its greatest concentration of smooth plains. We finish with a discussion of the "Central MIH" and "Central MUH" regions, which contain interesting plains albedo features as well as some of the best examples of small, fresh impact features. Note that here, and for the remainder of the paper, we use the abbreviations "MIH" and "MUH" to denote the Mariner-imaged and Mariner-unimaged hemispheres, respectively.

To assist in locating and comparing features in the MIH, we have reproduced (Fig. 3) a sketch map from the *Atlas of Mercury* (Davies et al., 1978) showing Mercury's major basins and ray systems as observed by Mariner 10. The mercurian coordinates of the rayed craters in Fig. 3 are also listed in Table 2. Those craters on this list that lack a proper name we designate by "MRC-#," where "MRC" stands for "Mariner Rayed Crater" and # is a number running from 1 to 7. Since one of our goals was to correlate the optical and radar "freshness" of these craters, we also list in Table 2 the USGS crater freshness class and a short description of the radar appearance.

Throughout our presentation of the images, we will make references to the earlier Goldstone-VLA images and maps. This not only provides some historical context, but also enables us to compare with images which were made at a different radar wavelength and which are free of north/south ambiguity. For this reason we have included, in Fig. 4, a contour map from

Butler (1994) showing radar reflectivity from Goldstone-VLA images mapped onto the Mercury coordinate grid. Recent advances have also been made in Earth-based optical telescopic imaging of the planet, and we will draw comparisons with these where appropriate.

3.1. Mariner-approach region

This region spans the terminator (∼10° W long.) as viewed by Mariner 10 when it approached Mercury in half-phase. Two Goldstone-VLA depolarized images (Slade et al., 1992; Butler et al., 1993) of the region are shown in Fig. 5. Aside from the polar features, the dominant features in Figs. 4 and 5 are Kuiper Crater (31.5° W, 11° S) on the MIH side (see Fig. 3) and the north and south midlatitude features located east of the terminator in the MUH. We refer to these southern and northern MUH features as "A" (347.5° W, 34° S) and "B" (343° W, 58° N), respectively, adopting the designation coined by Harmon (1997). Being at about the same longitude, these two features would merge into a single bump in a CW Doppler spectrum; together they account for one of Goldstein's two main SC Doppler features. The resolution of the VLA image (Fig. 5) was inadequate for determining the nature of these features. Butler et al. (1993), noting their rough circularity, referred to them provisionally as "basin" features. An Arecibo long-code SC image giving a view similar to that of Fig. 5b is shown in Fig. 6. Feature "A" and Kuiper stand out clearly in this image. Feature "B" can also be seen as an ambiguity foldover artifact. A better view of feature "B" can be seen in Fig. 7, which is the image formed from the same data as in Fig. 6, but where the mapping solution is for the region north of the Doppler equator.

Table 2
Mariner rayed craters

Name	Longitude	Latitude	Diameter (km)	Class	Radar appearance
Kuiper	31.5	−11.0	60	c_5	Bright rim + rays
MRC-1	49.5	−29.0	22		Bright floor and rim
MRC-2	50.3	+21.5	30	c_4	Bright rim
MRC-3	64.8	+1.2	40	c_5	Bright rim
Tansen	71.0	+4.0	25	c_5	Bright rim
Snorri	83.5	−8.5	20	c_5	Bright rim
Copley	85.7	−37.7	30	c_5	Bright rim
MRC-4	101.0	−13.2	15	c_5	Bright rim
MRC-5	105.7	−8.5	12	c_5	V. bright rim + fan
Ives	111.9	−32.6	20	c_5	Bright rim
MRC-6	117.2	+27.6	45	c_4	Bright rim + rays
Mena	125.0	+0.1	20	c_5	No obvious feature
Degas	126.8	+37.5	45	c_5	Bright floor + rays
Schoenberg	136.2	−15.7	30	c_5	Bright floor
MRC-7	157.0	−16.6	17		Bright rim + single ray
Bashō	170.0	−32.0	70	c_5	Bright floor + rays
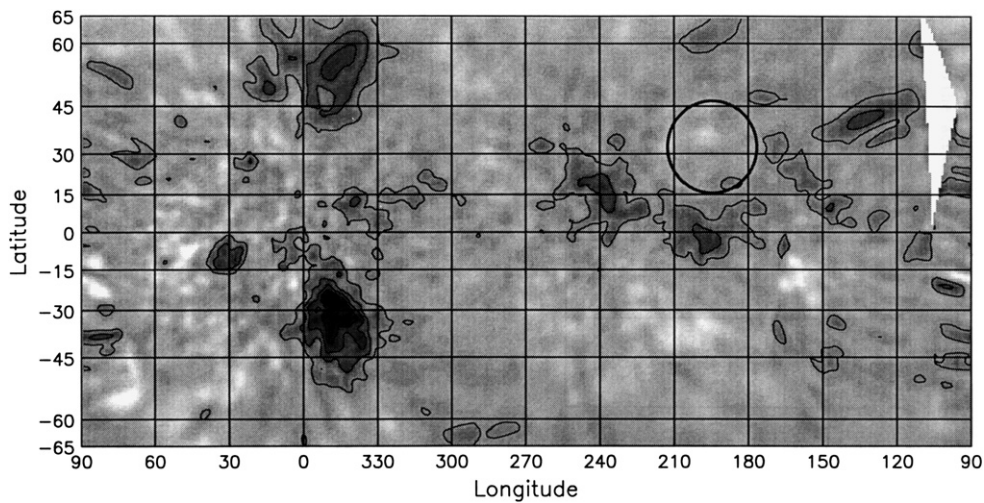
Fig. 4. Radar brightness contour map (SC polarization) of Mercury from Goldstone-VLA observations. Darker shading denotes higher radar brightness. The rim of Caloris Basin is shown (circle). The figure is from Butler (1994).
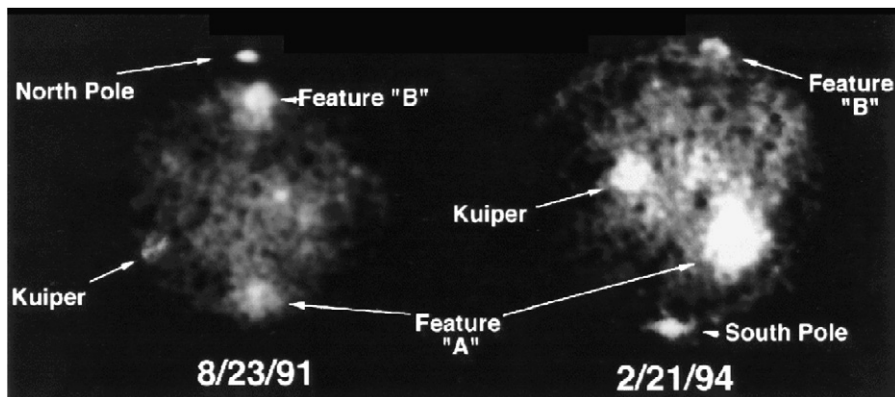
Fig. 5. Goldstone-VLA radar images (SC polarization) of Mercury from observations on (left) August 23, 1991 (sub-Earth point at 353.5° W, 11.0° N), and (right) February 21, 1994 (sub-Earth point at 15.7° W, 10.6° S).

3.1.1. Feature "A"

The best pre-upgrade Arecibo images (Harmon, 1997) showed "A" to be a rayed impact feature associated with an 85-km-diameter crater (347.5° W, 34° S), placing it in the same class as the lunar crater Tycho in terms of size and freshness. The new Arecibo images not only confirm this, but also show considerably more detail (Fig. 8). Based on its brightness and complex, pristine structure, this appears to be the freshest
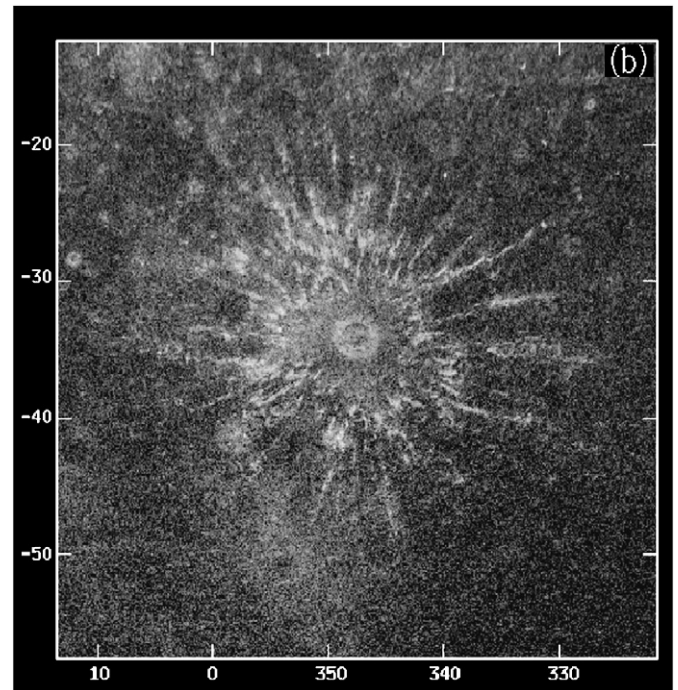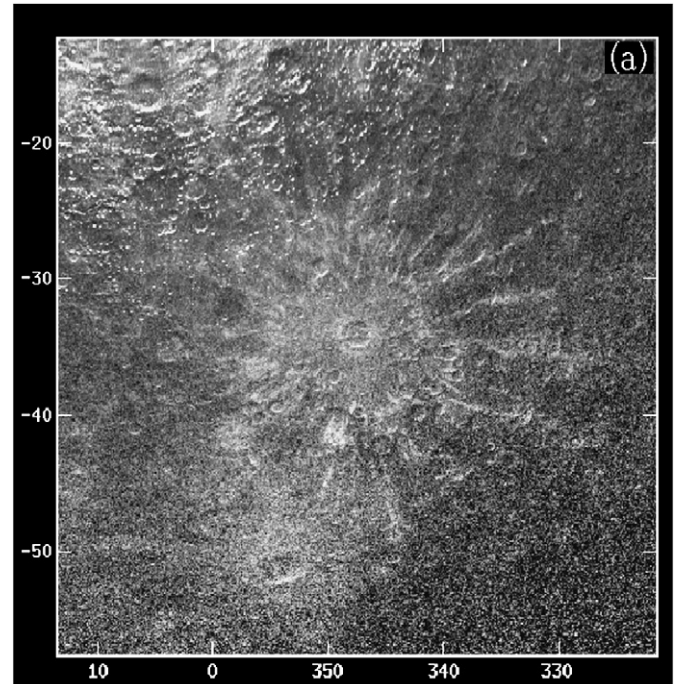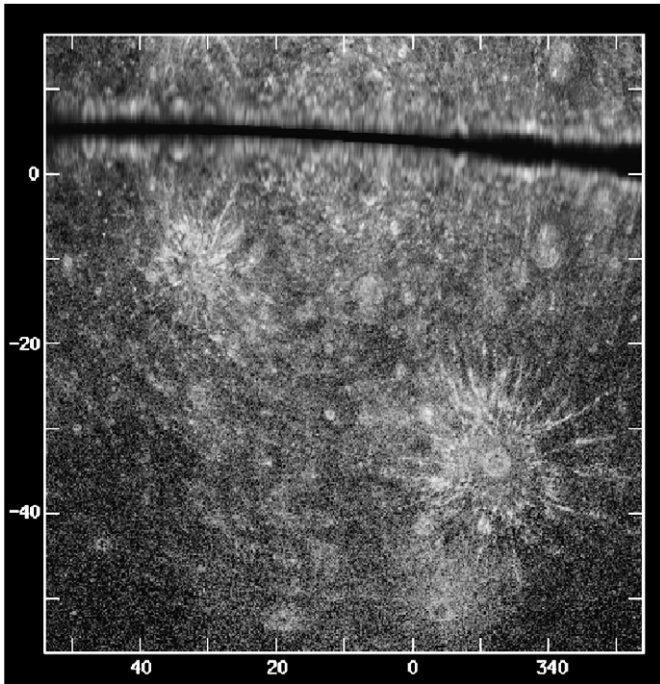
Fig. 6. Arecibo image (SC polarization) of the southern portion of the Mariner-approach region. The observations are from June 1–3, 2001. The Doppler equator corresponds to the dark swath at top. The Mariner 10 approach terminator approximately bisects the image vertically. The dominant features are Kuiper Crater in the upper left and "A" in the lower right. N/S-ambiguity foldover from feature "B" appears at bottom (south of "A"). $\sigma^{\circ}_{\rm sc}({\rm max.}) = 0.0517$.
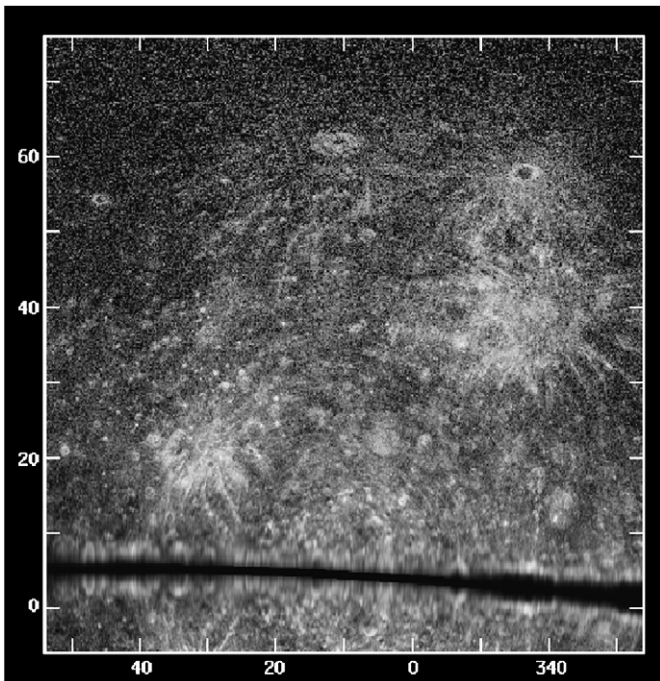

Fig. 7. Same as Fig. 6, except covering the region north of the Doppler equator. The dominant features are "B" (upper right), a large rayed crater west of "B" (upper center), and a cluster of small craters (left center). Note also the ambiguity foldover from Kuiper (below the cluster) and from "A" (below "B"). $\sigma^{\circ}_{\rm sc}({\rm max.}) = 0.0560$.

Fig. 8. Arecibo image of feature "A" in the (a) OC and (b) SC polarizations. The OC image is from June 1–3, 2001. The SC image is from June 1–2, 2001 and May 14, 2002. $\sigma^{\circ}_{\rm sc}({\rm max.}) = 0.0622$.

large impact on the planet. It is also arguably the most spectacular radar crater feature in the Solar System, its only rival being Tycho. Although the rays are not as long as those seen in X-band ($\lambda 3.8$-cm) radar images of Tycho (Zisk et al., 1974), the ray/ejecta system is much more elaborate. The new OC image (Fig. 8a) shows a central 85-km-diameter crater with a central peak. Extending about one crater radius beyond the crater rim is a bright collar that shows up best in the SC image. Beyond

this is a fainter bright halo extending out another two crater diameters. The periphery of this halo shows a bright fringe made up of short ray segments, within which are nested a number of craters of 20–40 km diameter. These craters are either secondaries from the main impact or pre-existing craters whose outlines are enhanced by the bright ejecta; given the size of these craters, the latter is more likely. Extending beyond the halo are numerous longer rays up to 400 km in length. A few of these rays, especially in the northeast, show some curious parallel pair structure; since this shows up best in the OC, it is possible that this reflects some topographic relief associated with the rays or the two sides of crater chains. The extent of the halo and rays roughly agrees with the size of the feature in the Goldstone-VLA images (Fig. 4). The radar rays stop just short of the Mariner 10 terminator, and any optical rays that might extend further into the MIH would be difficult to see in the Mariner images owing to the low Sun angles. Thus, it is not surprising that there was no hint of this feature in the Mariner images. Earth-based telescopic images (Warell and Limaye, 2001; Mendillo et al., 2001) show modestly elevated optical brightness from the general vicinity, but no distinct feature stands out.

3.1.2. Feature "B"

The pre-upgrade Arecibo SC images of this feature showed a rather amorphous circular feature with a small, slightly irregular, central dark spot (Harmon, 1997). This appearance, and the dissimilarity to feature "A," left some doubt as to the true nature of this structure. The possibility of "B" being a shield volcano was even considered (Harmon, 1997). However, the new images indicate that "B" is an impact structure. This can be seen from Fig. 9, which shows an image derived from the same observations as those used for Fig. 7. The central feature now shows a circularity consistent with a 95-km-diameter impact crater (343° W, 58° N) with a bright rim ring. The circularity of the crater is most visible in the OC image, while the bright rim is more pronounced in the SC image. Some streaks and patches are seen to the south and west that appear to be ejecta rays similar to, but less distinct than, those from "A." The OC image shows some smaller bright crater features that may be secondary craters or fresh primaries. The source crater shows no central peak (unlike "A"), although this is not unusual for mercurian craters of this size. Instead, there appears to be a N/S-trending lobate or terrace structure on the west side of the crater floor. This structure is radar-bright in the SC, which probably accounts for the noncircularity noted in the pre-upgrade images. The asymmetries in "B" crater may be associated with wall slumping, irregular crater floor roughness, or pre-impact topography. Asymmetric crater rims and ejecta can also be caused by oblique impact, as has been seen for the Moon and Venus (Hawke and Head, 1977; Herrick and Forsberg-Taylor, 2003). An oblique impact might explain the fact the rays from "B" are concentrated preferentially in the south and west. The OC image shows some highlighting and shadowing suggestive of an upraised crater rim edge, which would give further support for this being an impact crater and not a volcanic caldera.
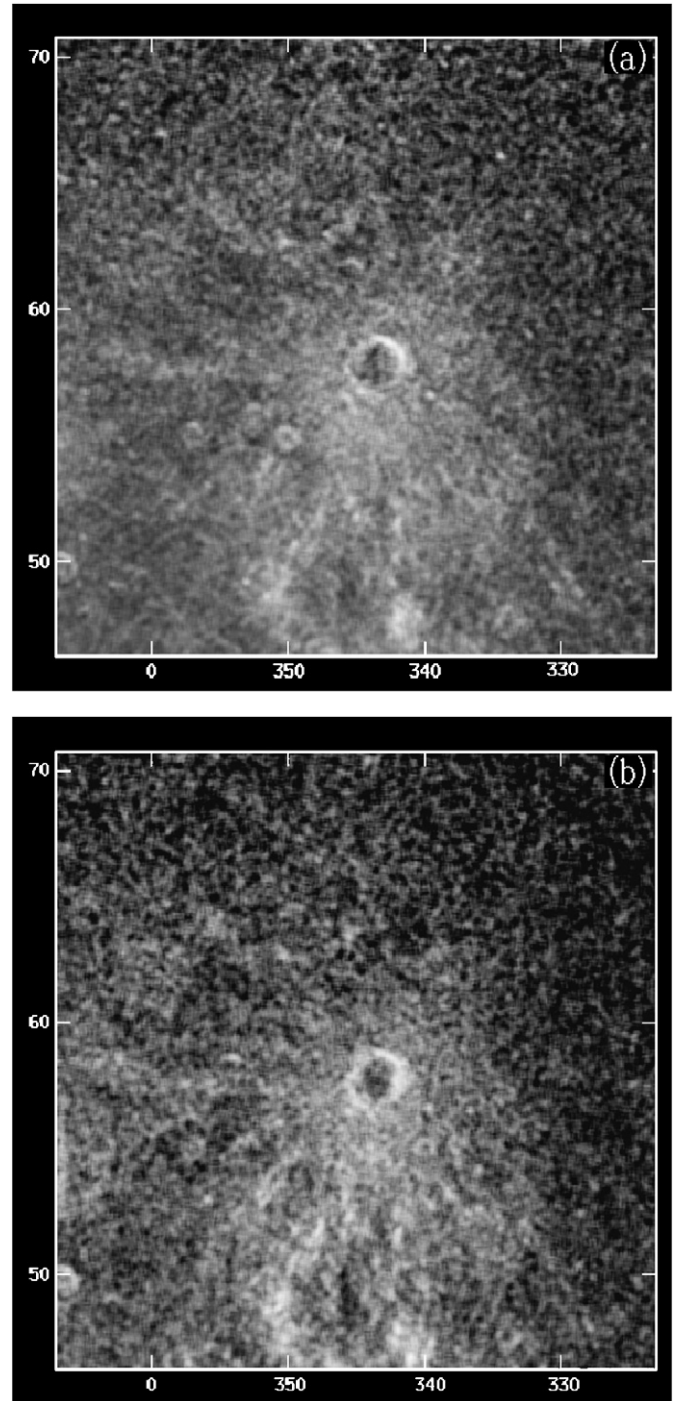

Fig. 9. Arecibo image of feature "B" in the (a) OC and (b) SC polarizations. The data are from June 1–3, 2001. A 5×5-pixel smoothing was applied to reduce noise. $\sigma_{\mathrm{SC}}^{\circ}(\mathrm{max.}) = 0.0316$.

3.1.3. Kuiper

Kuiper was not only the most prominent bright crater in the Mariner-approach images, but also the brightest mercurian feature seen by Mariner (Hapke et al., 1975; De Hon et al., 1981). It has even been identified as a bright spot in Earth-based optical telescopic images (Warell and Limaye, 2001). Kuiper can be seen in Fig. 10, which shows the Mariner image mosaic of the H-6 (Kuiper) quadrangle located west of the
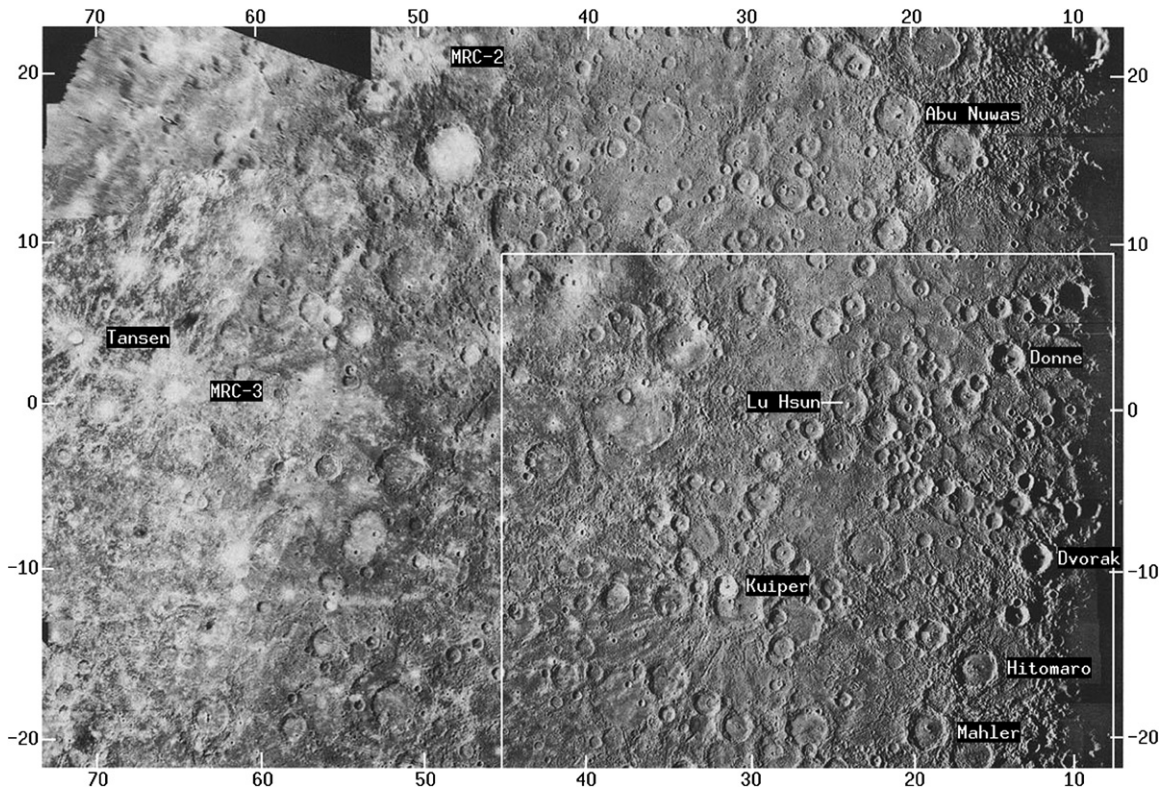
Fig. 10. Mariner 10 image mosaic of the H-6 (Kuiper) quadrangle of Mercury, with labels denoting craters referred to in the text and a box showing the north, east, and west boundaries of the image in Fig. 11. The Mariner-approach terminator is the dark edge on the right. Adapted from the Atlas of Mercury (Davies et al., 1978).
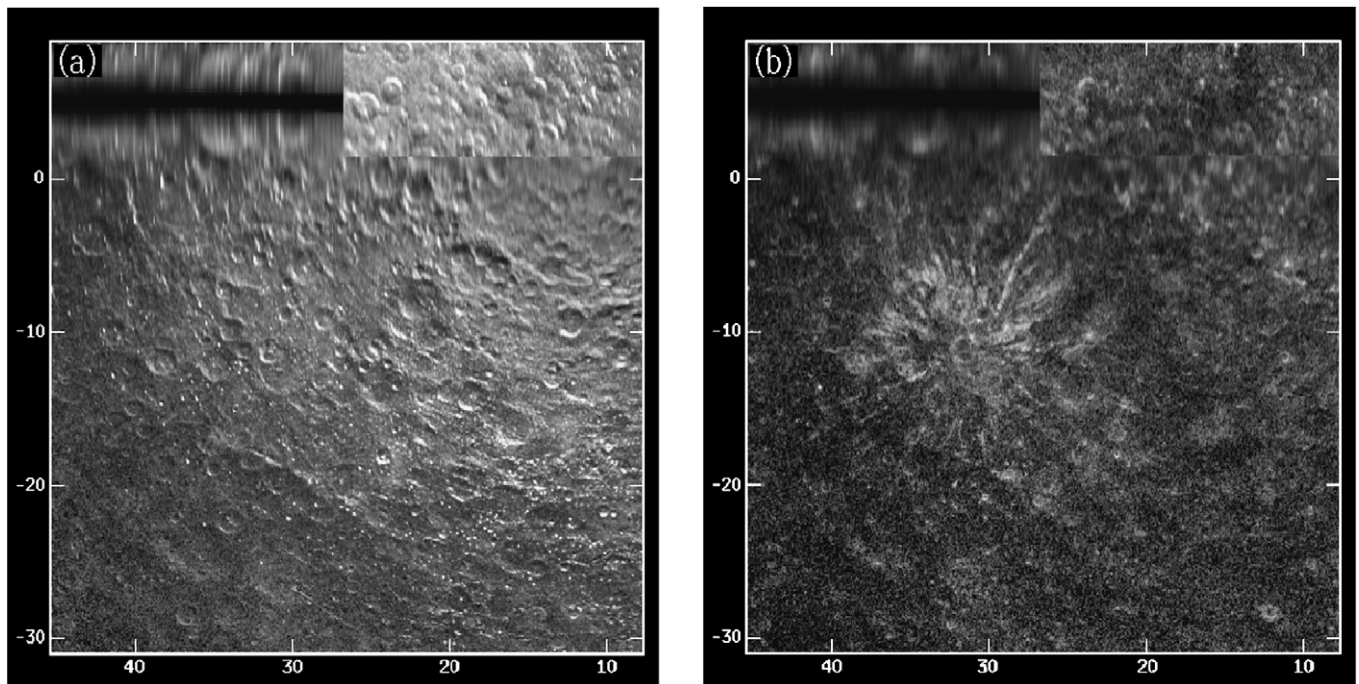

Fig. 11. Arecibo image of the southeast portion of the H-6 quadrangle in the (a) OC and (b) SC polarizations. The image location is shown by the box in Fig. 10. The data are from June 1–3, 2001, with a strip insert at top right from April 14–17, 2004. Kuiper Crater is at center left at 31.5° W, 11° S and Dvorak Crater is located at 12.5° W, 9.5° S. σ°_{sc}(max.) = 0.0775.

approach terminator. Presumably, this c_5-class crater (31.5° W, 11° S) is one of the freshest impacts on the planet. This structure appears fresh to the radar as well, as evidenced by the prominent bright ejecta and rays seen in the SC radar image in Fig. 11. There is also some enhanced SC echo from the floor of the c_4-class Murasaki Crater just to the southeast of Kuiper.

There is good correlation between the optical and radar rays west of Kuiper crater. The most prominent radar ray, which runs NNE of the crater, coincides with a faint optical ray segment that crosses another prominent crater at 29° W, 6° S. The radar ejecta show an asymmetry in that the brightest rays are concentrated north of the crater. This may be indicative of an oblique impact or of a focussing of the ejecta by pre-existing topography (since the Kuiper impact landed squarely on the rim of the older crater Murasaki). The crater does, in fact, have a non-circular shape that is apparent in both the Mariner and OC radar images. Note the lack of ejecta features in the OC image, which is dominated by specular reflection at these incidence angles. Note also the trailing off of the specular contribution toward the lower left of this image, where the incidence angles are greatest and diffuse scatter starts to dominate. The Goldstone-VLA image of Kuiper (Slade et al., 1992; Butler et al., 1993) showed a prominent ejecta pattern in the OC polarization, but that was at higher incidence angles where diffuse scattering dominates.

3.1.4. Other fresh (c_5) craters

Kuiper is just one of close to a score of "fresh" c_5-class craters in the USGS H-6 quadrangle (De Hon et al., 1981). Several of the larger of these happen to be clustered just west of the Mariner 10 terminator between 13° W and 24° W longitude (see Fig. 10). Interestingly, none of these craters show radar rays or any other strong radar signature, as can be seen from inspection of the east side of the SC image in Fig. 11b. Only Hitomaro Basin (16° W, 16° S) shows much of a feature, namely, a moderately bright floor and surrounding dark halo. Other c_5 craters in this region, such as Mahler (19° W, 19° S), Dvorak (12.5° W, 9.5° S), Donne (14° W, 3° N), Lu Hsun (23.5° W, 0.5° N), and Abu Nuwas (21° W, 17.5° N) show little or nothing in SC. Although we will later show other examples of c_5 craters lacking strong radar features, this lack of correlation may be strongest here. This is perhaps not surprising, given that the deep shadows cast near the terminator (see Fig. 10) will tend to accentuate a crater's apparent freshness (by highlighting secondary craters and hummocky ejecta), whereas optical rays (which correlate better with "radar freshness") are difficult to observe at such low Sun angles. Also, as we shall see, there is a tendency for large c_5 craters to have weaker radar features than smaller c_5 craters.

3.1.5. Smaller bright craters

Apart from "A," "B," and Kuiper, all of the bright SC radar features in this region are found to come from small craters. The brightest SC feature near the terminator in Fig. 11 comes from a 30-km-diameter crater at 12° W, 28° S, near the SW rim of Dario Crater. This crater is not classified in the H-11 geologic map of Trask and Dzurisin (1984), and the extremely low Sun angle prevents a search for optical rays. This crater shows no radar rays, but rather exhibits the distinctive bright rim-ring or collar that we have found to be the most common SC feature of small radar-bright mercurian craters. A closeup of this crater is shown in Fig. 12a. The rim-ring starts just inside the inner rim base and extends about one crater radius beyond the rim.

Another small crater feature of interest is located at 339° W, 12° N, midway between "A" and "B." This appears as a small but prominent bright spot in the X-band VLA images (Figs. 4 and 5). A closeup S-band image is shown in Fig. 12b. This shows a 12-km-diameter crater with an SC rim-ring and no radar rays.

In several places on Mercury, we have found loose clusters of small bright craters that do not appear to be secondaries from larger impacts. One such cluster is centered at 28° W, 30° N. Although this cluster can be seen in Fig. 7, the closeup image in Fig. 13 comes from more recent observations in April, 2004. Most of the spots can be traced to craters 3–15 km in size, while two adjacent unresolved spots near 27° W, 29° N coincide with two craterless or otherwise unresolved bright spots in the Mariner images. The larger features appear as rings in SC. The cluster lies in a rather craterless "intermediate plains" region that is described as "probably lava flows" in the H-2 geologic map (McGill and King, 1983). Also visible at the bottom of Fig. 13 is a faint circular feature centered on 23° W, 23° N from the rim of Ts'ai Wen-Chi Crater. The combination of this feature and the crater cluster to its north and northwest may account for the SC feature that can be seen at this location in the VLA map (Fig. 4) and which is mentioned in Butler et al. (1993). There is also evidence for a bright optical feature at this location in Earth-based telescopic images (Warell and Limaye, 2001; Mendillo et al., 2001).

3.1.6. Other features

One other feature of note is a large structure centered at 11° W, 62° N, to the west of feature "B" in Fig. 7. This region was not imaged by Mariner 10. At the center of this feature is a large central crater (140 km diameter) with a bright floor and dark halo. Outside the dark halo is a large and diffuse bright halo, with filamentary rays extending to the southwest. The high incidence angle may account for the faintness of the feature. It is likely that this feature and its southern rays and ejecta account for the bright contours extending west of "B" in the Goldstone-VLA map (Fig. 4). A similar large crater with bright floor, dark halo, and brighter outer halo is centered near 340° W, 9° S in Fig. 6. This crater is about 200 km in diameter. This feature can also be seen in the images presented in Section 3.5.

3.2. Trans-Caloris region

We use the term "trans-Caloris" to refer to the region of the MUH to the west of Caloris Basin. One of the original Goldstone-VLA images (Slade et al., 1992) was centered on this region. This X-band SC image is shown in Fig. 14. The dominant feature in the VLA image is the large irregular patch located just north of the equator at 240° W longitude. This must be the source of the second "Goldstein feature" (Goldstein, 1970, 1971). Following Harmon (1997), we refer to this as feature "C." The VLA image also shows a bright patch SE of "C" and a small bright spot NW of "C." A large-scale OC/SC image pair from 2001 Arecibo S-band data is shown in Fig. 15. Feature "C" dominates the SC image, although several other features can also be seen, as discussed below.
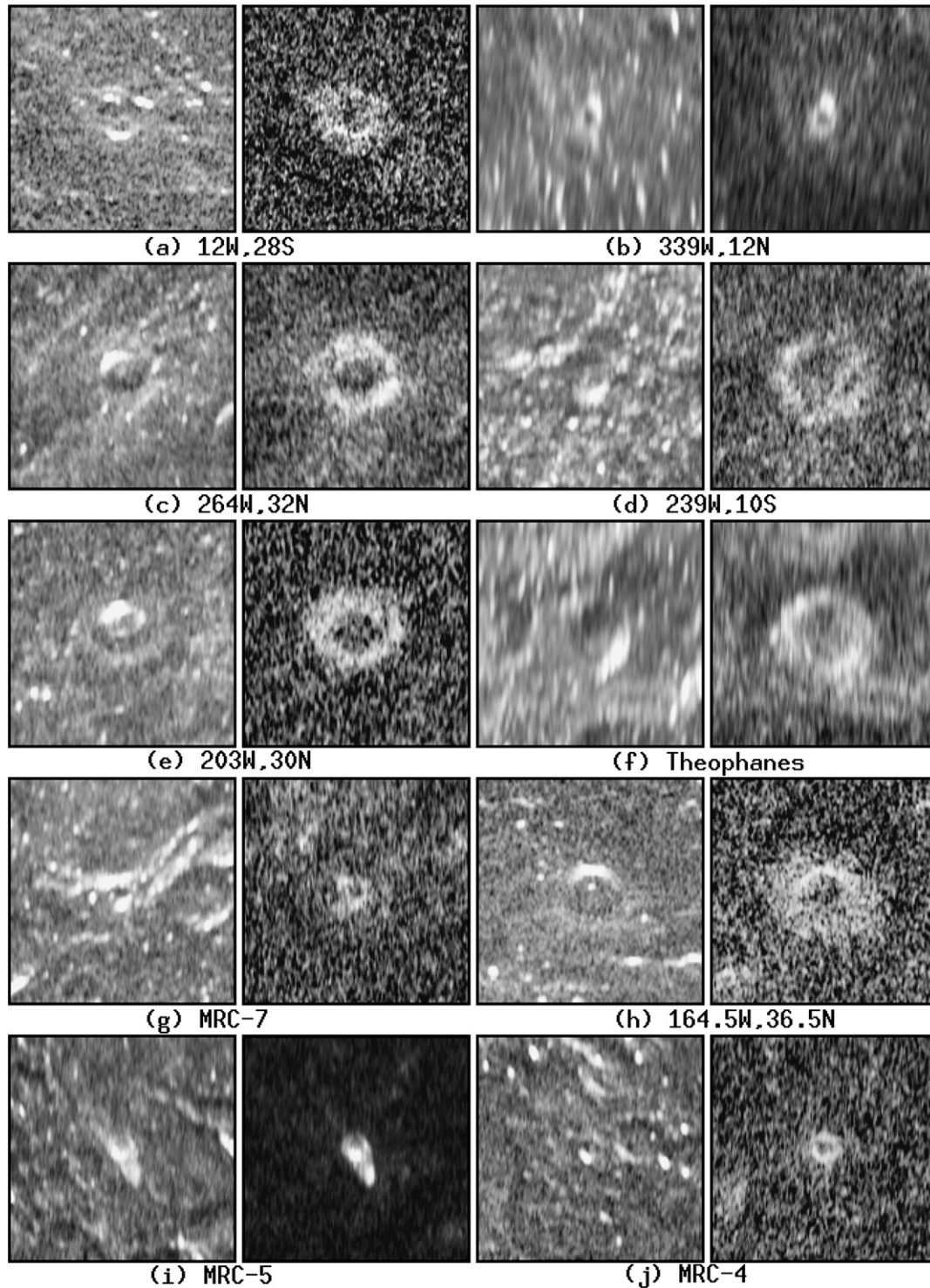
Fig. 12. Arecibo closeup image pairs (OC on left, SC on right) for small to medium-size radar-bright craters. Each image measures $4° \times 4°$. The crater names/locations and σ°_{sc}(max.) values (in parentheses) are as follows: (a) 12° W, 28° S (0.0584); (b) 339° W, 12° N (0.0794); (c) 264° W, 32° N (0.109); (d) 239° W, 10° S (0.0845); (e) 203° W, 30° N (0.0999); (f) Theophanes (0.0577); (g) MRC-7 (0.0537); (h) 164.5° W, 36.5° N (0.0783); (i) MRC-5 (0.292); (j) MRC-4 (0.101); (k) Snorri (0.112); (l) Futabatei and companion crater to the north (0.0751); (m) MRC-3 (0.0657); (n) MRC-2 (0.0538); (o) MRC-1 (0.0763); (p) 102.5° W, 19° S (0.0683); (q) 284° W, 3° S; (r) 272° W, 14° S (0.0917).

3.2.1. Feature "C"

Feature "C" is one of the most prominent SC radar features on the planet, even showing up as a bright spot in Earth-based telescopic images (Warell and Limaye, 2001; Mendillo et al., 2001). Nevertheless, characterizing "C" on the basis of the S-band images has been difficult owing to its proximity to the Doppler equator and the less-than-optimal planet distance at those times when this longitude was visible from Arecibo. The
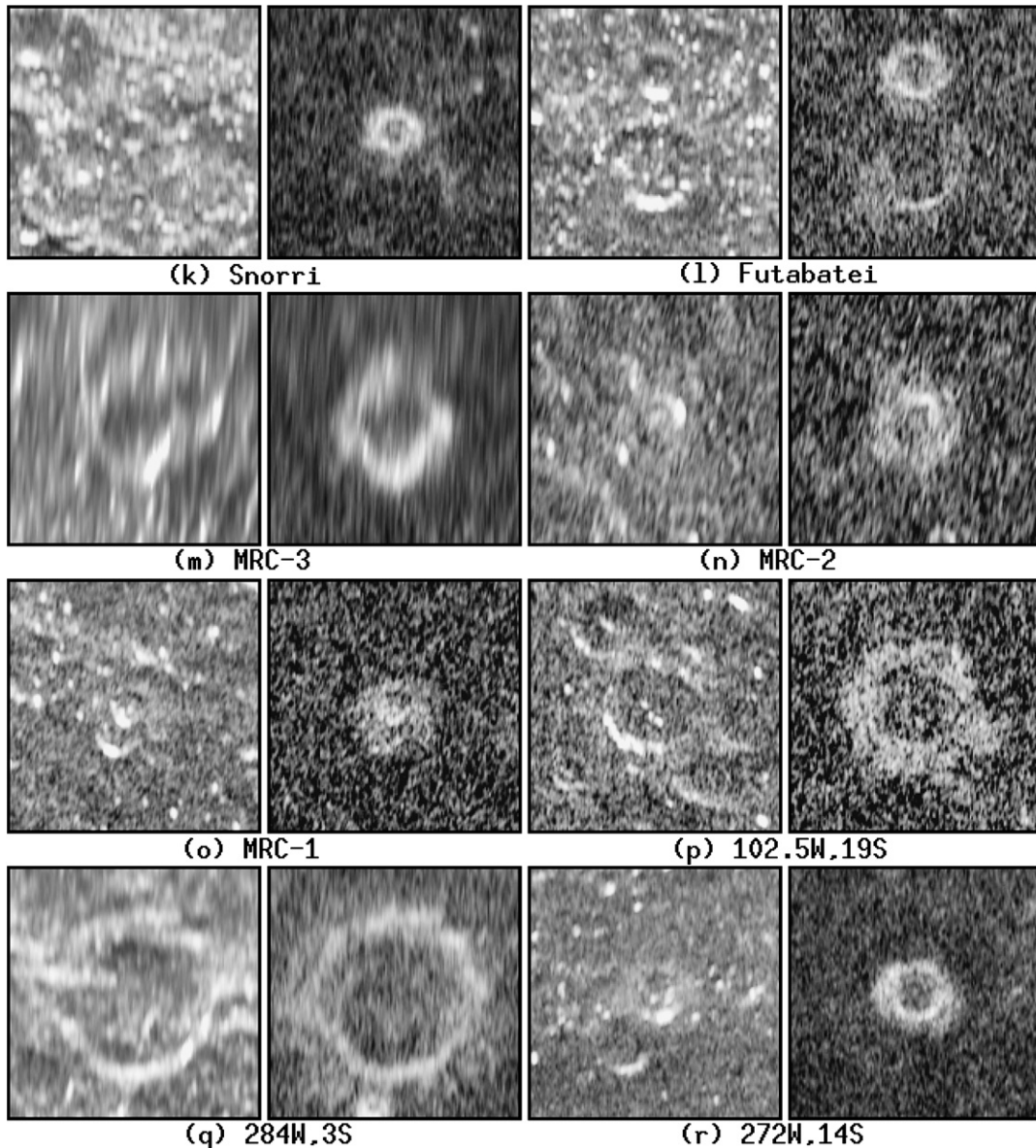
Fig. 12. (*continued*)

best of the early (2001) SC images (Fig. 16a) showed many bright ring features suggestive of a cluster or swarm of small, fresh impacts rather than a single dominant impact. This was also consistent with the highly irregular shape of the feature in the VLA image. However, more recent images now reveal the presence of a large central source crater at 246° W, 11° N. An SC image from 2004 showing this crater is shown in Fig. 16b. This shows the crater's rim-ring and surrounding dark halo, albeit split by the Doppler equator. We then went back and found weak images of the central crater from observations in late April 2002, when the planet was at a less favorable range but when the Doppler equator was farther south. This OC/SC pair is shown in Fig. 17. The OC image, though poor, shows a 125-km-diameter crater with a bright central peak and a terrace on the eastern interior rim wall. The SC image shows the rim ring and dark halo. Additional evidence for this being the

"C" source crater comes from the fact that ray features embedded in the ejecta (see Figs. 16a and 16b) appear to radiate from this crater. However, the Arecibo images indicate that "C" is an asymmetric feature, with the preponderance of bright ejecta lying to the north of the source crater. This would be consistent with the location and irregular shape of the feature in the VLA image (see Figs. 4 and 14). Finally, it is important to note that our proposed source crater coincides exactly with the location of a ring feature in one of the old (pre-Mariner) radar maps of Zohar and Goldstein (1974). This is one of several circular features noted by Zohar and Goldstein as being evidence for Mercury cratering. The possible association of this feature with the larger feature "C" had been suggested earlier by Butler et al. (1993) and Butler (1994). However, Butler et al. also suggested that "C" might be a circum-Caloris smooth plains feature similar to that seen due south of Caloris in Tir Planitia. Al-
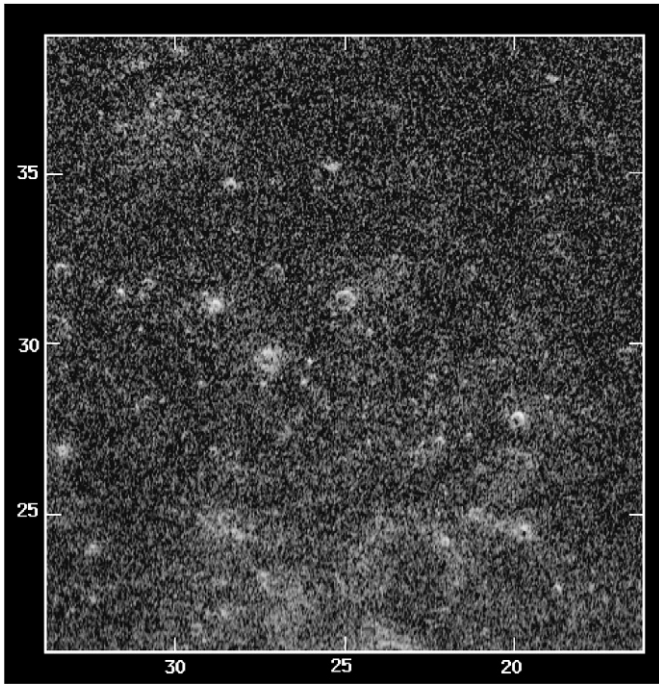
Fig. 13. Arecibo image (SC polarization) of a cluster of small bright craters SSE of Holbein. The data are from April 14–17, 2004. $\sigma_{sc}^{\circ}(\text{max.}) = 0.124$.
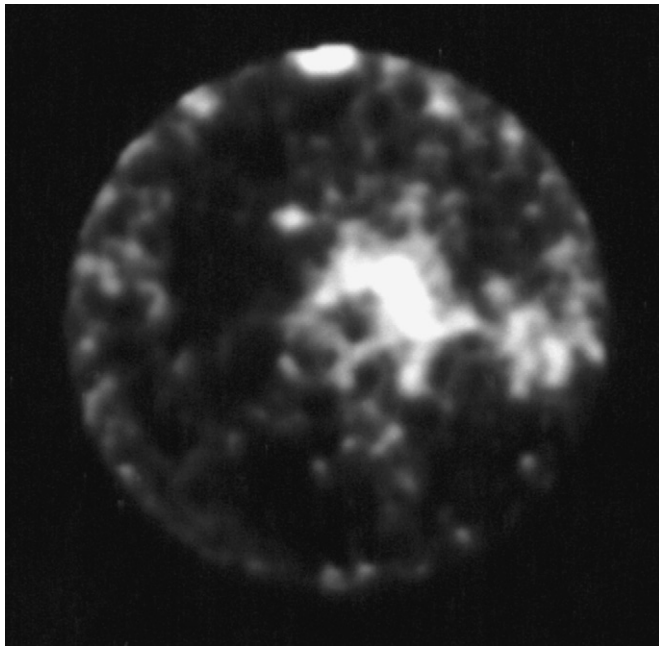

Fig. 14. Goldstone-VLA radar image of Mercury (SC polarization) from August 8, 1991 (sub-Earth point at 253° W, 11° N). Feature "C" is the large irregular bright structure just right of center, and the small bright spot just to its NW is the crater in Fig. 12c. The bright spot at top is the north polar ice feature. This image originally appeared in Slade et al. (1992).
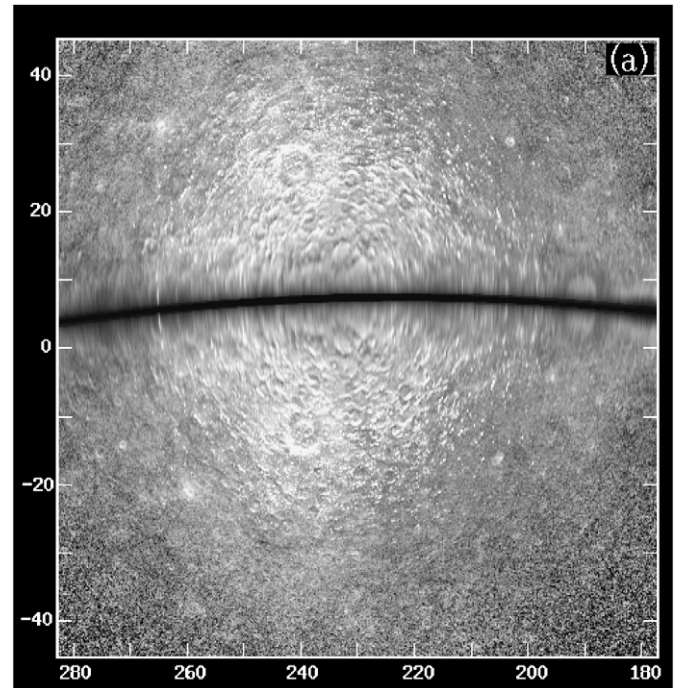

Fig. 15. Arecibo radar image of the "trans-Caloris" region of Mercury in (a) OC and (b) SC polarizations. The data are from July 7–8, 2001. $\sigma_{sc}^{\circ}(\text{max.}) = 0.0551$.

though this would seem to be a reasonable hypothesis based on Fig. 4, the Arecibo data now show that the feature "C" locale is heavily cratered (see Fig. 15a), not smooth plains, and that feature "C" itself is almost surely ejecta from the source crater at 246° W, 11° N.

3.2.2. "Ghost feature"

In the large-scale SC image (Fig. 15b), one can see a large faint feature due south of "C." There is a hint of the northeastern part of this feature in the VLA image (Fig. 14) as well as in telescopic images (Warell and Limaye, 2001). A closer view of the feature is shown in Fig. 18; here we use an OC image from April 2002 and an SC image from August 2004. This feature resembles a faint version of feature "A."
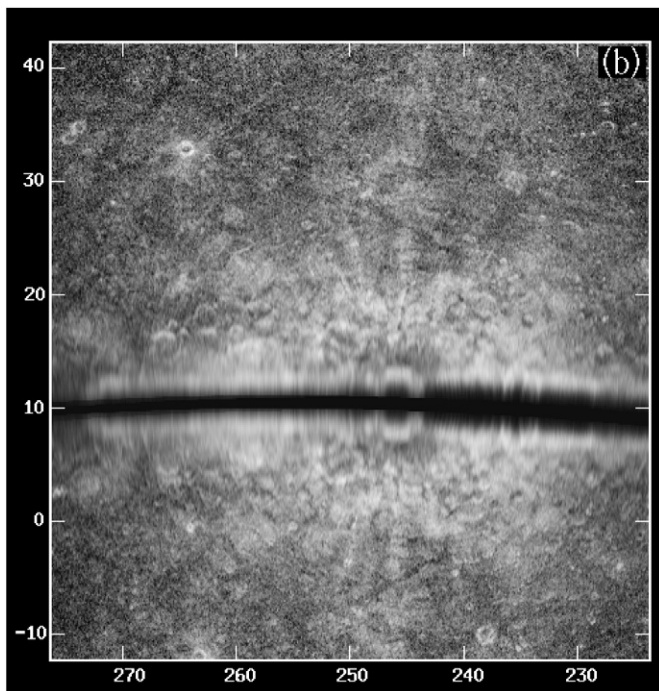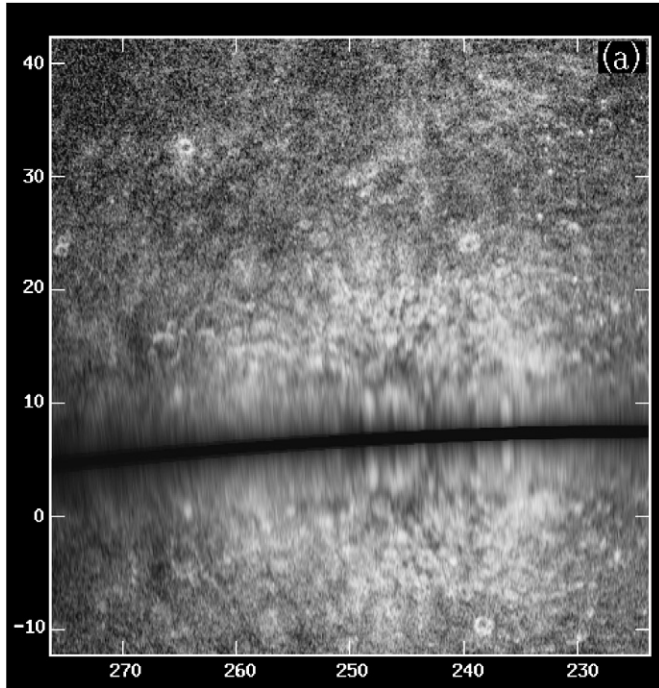
Fig. 16. Arecibo radar images (SC polarization) of the feature "C" region from observations on (a) July 7–8, 2001 and (b) August 8–9, 2004. σ_{SC}°(max.) = 0.0634 (a) and 0.0898 (b).
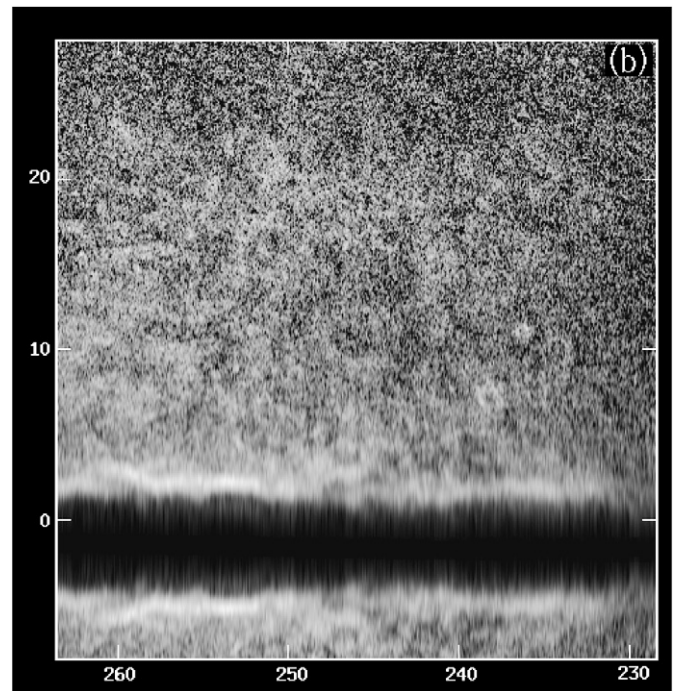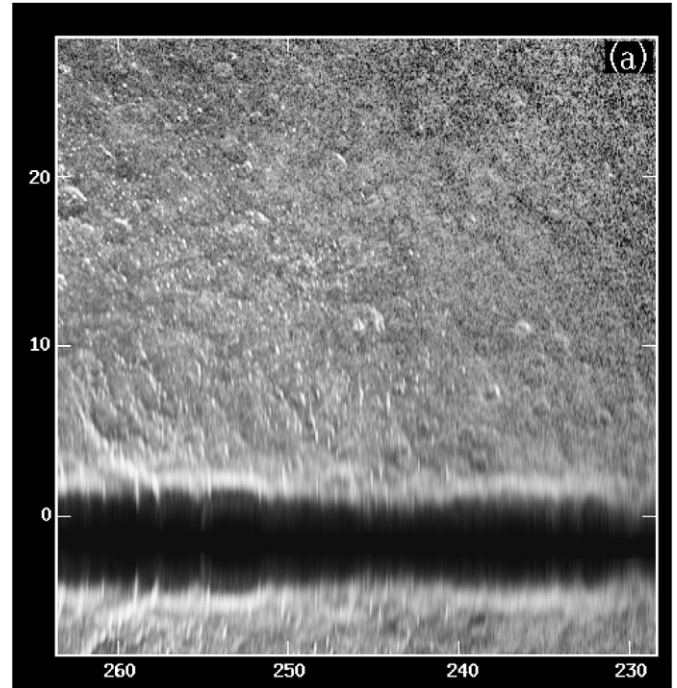
Fig. 17. Arecibo radar images of the feature "C" source crater in (a) OC and (b) SC polarizations. The data are from April 22–30, 2002. The crater center is at 246° W, 11° N. σ_{SC}°(max.) = 0.0906.

The OC image (Fig. 18a) reveals an 85-km-diameter central crater at 242° W, 26.5° S, while the SC images (Figs. 18b and 15b) show a bright rim collar surrounded by a dark halo and outer filigree of faint rays. We consider it most likely that in this "ghost feature" we are seeing a moderately fresh impact that is in an intermediate state of degradation or maturity.

3.2.3. Small bright craters

Fig. 15b shows several small, isolated bright craters. After resolving the N/S-ambiguity, we find the most prominent of these to be located at: 264° W, 32° N; 239° W, 10° S; 271° W, 14° S; and 203° W, 30° N. All four of these appear as ring features in SC. Three of these craters are shown in closeup in Figs. 12c–12e. Note particularly the first one (264° W, 32° N); this impact shows a prominent rim collar extending 1.3 crater
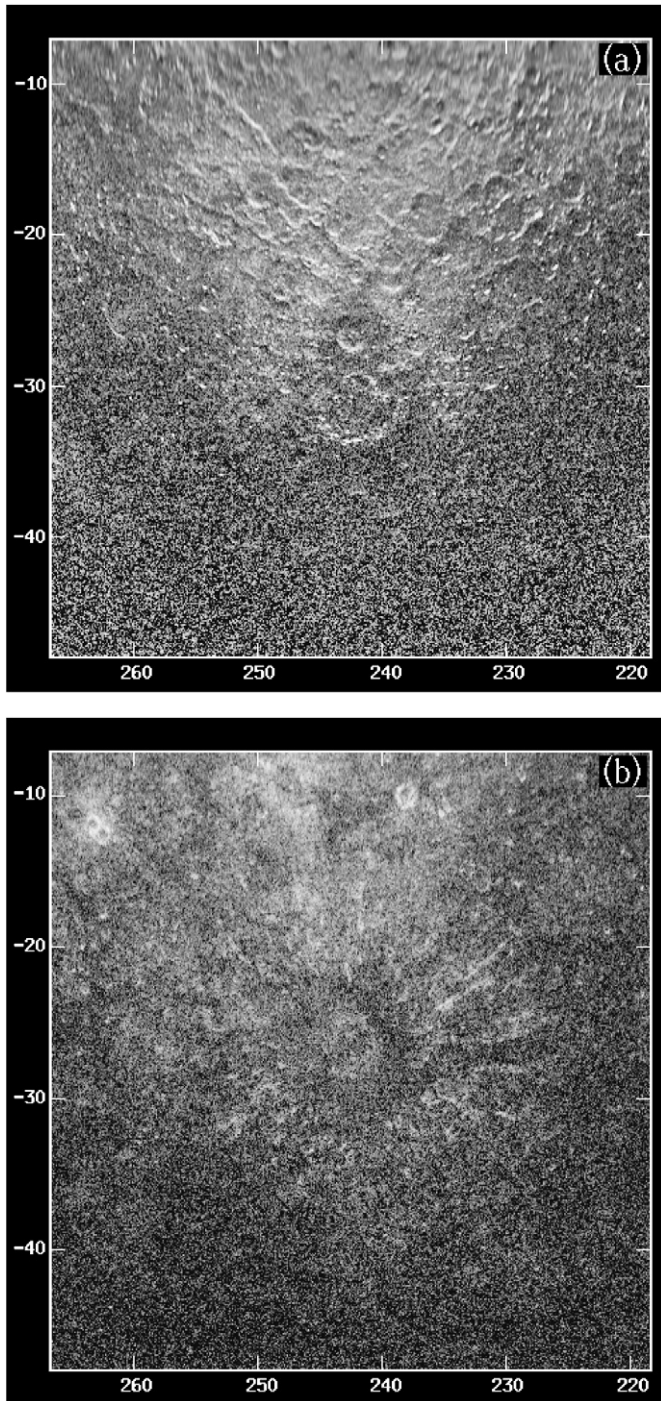
Fig. 18. Arecibo radar images of the "ghost crater" south of "C" in (a) OC and (b) SC polarizations. The OC image is from April 22, 2002 and the SC image is from August 8–9, 2004. The crater center is at 242° W, 26.5° S. $\sigma^\circ_{\text{sc}}(\text{max.}) = 0.0674$.

ently lies in the western (Mariner-unimaged) floor of Caloris Basin; a closeup of this crater is shown in Fig. 12e. Although this crater feature is not apparent in the VLA images, it does coincide with a bright spot in telescope images (Warell and Limaye, 2001). Finally, note the cluster of small bright spots near 230° W, 34° N that resembles the small-crater cluster in Fig. 13. There is a corresponding bright patch just north of "C" on the VLA map (Fig. 4).

3.2.4. Other features

We have found a two-ring basin at 241° W, 27° N. This is clearly seen in the OC image in Fig. 15a. This basin has an outer rim of 250-km diameter and an inner ring of 115-km diameter, making this very similar in size and form to the two-ring basins Renoir and Michelangelo. The SC images show the basin floor to be mostly radar-dark.

Also worth noting in Fig. 15 is some bright structure to the east of "C." Multi-image comparisons show that the brightest part of this structure comes from just south of the Mercury equator at ∼210° W longitude. This correlates with the bright SC features SE of "C" in the VLA image (Figs. 4 and 14). Its location suggests that it may be coming from an MUH extension of the circum-Caloris smooth plains. This will be discussed further in the next section.

3.3. Caloris region

Here we discuss the general region around (and including) Caloris Basin, with an emphasis on the MIH region east of the 190° W Mariner departure terminator. This region is covered by the USGS H-8 (Tolstoj) map quadrangle and the western portions of the H-3 (Shakespeare) and H-12 (Michelangelo) quadrangles. We will also refer to the corresponding USGS geologic maps: H-8 (Schaber and McCauley, 1980), H-3 (Guest and Greeley, 1983), and H-12 (Spudis and Prosser, 1984). The dominant features in the Mariner images are the huge Caloris Basin and the vast smooth plains provinces that surround the basin.

Our best large-scale SC view of the region is shown in Fig. 19, which derives from Arecibo 10-μs long-code observations on June 9–10, 2002. In Fig. 20 we show a more recent (2005) SC image centered farther west on Mozart Crater. In Figs. 21 and 22 we show images from standard-code observations on August 16–17, 1998 and July 25–26, 1999; these images are useful for N/S-ambiguity checks, and also illustrate the limitations imposed by Doppler overspread aliasing in standard-code.

3.3.1. Caloris Basin

It is notable that Caloris, despite being the most prominent impact structure seen by Mariner 10, shows no obvious large-scale SC radar features. This was evident earlier from the X-band Goldstone-VLA imaging shown in Figs. 4 and 14 (Slade et al., 1992; Butler et al., 1993; Butler, 1994), as well as from the pre-upgrade Arecibo images (Harmon, 1997). The post-upgrade Arecibo images also show no bright SC features from Caloris. This is seen from the radar-dark appearance of
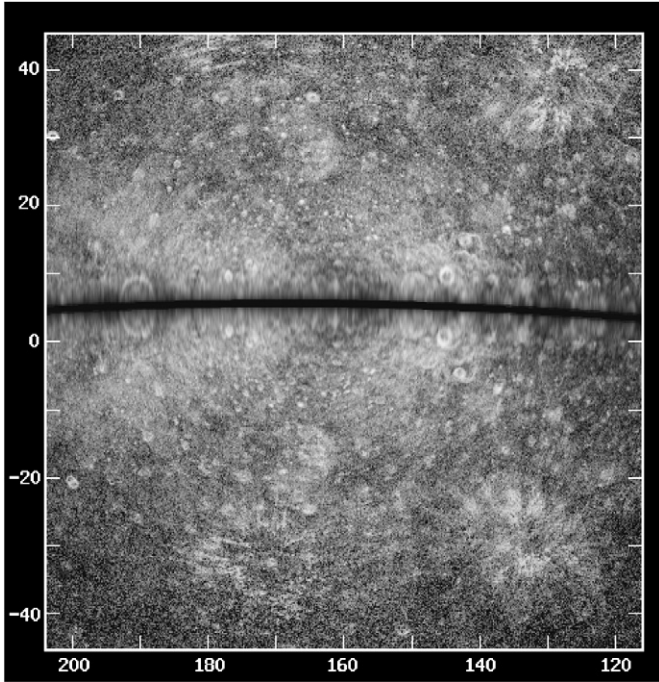
radii beyond the rim (see Fig. 12c), some bright extended ejecta to the south and east, and one long faint ray that extends to the NE (see Fig. 16b). This is the only one of these craters that shows up in the VLA image (Figs. 4 and 14), where it appears as a small bright spot; it also corresponds to a modest bright feature in telescopic images (Warell and Limaye, 2001). The easternmost of these three craters (203° W, 30° N) appear-

Fig. 19. Arecibo radar image of the circum-Caloris region (SC polarization) from observations on June 9–10, 2002. σ°_{SC}(max.) = 0.0537.
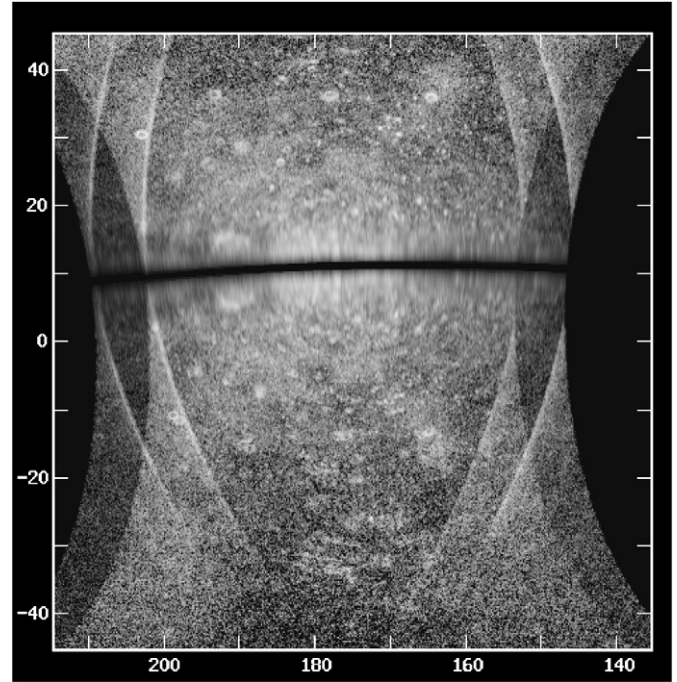

Fig. 21. Arecibo radar image of the circum-Caloris region (SC polarization) from standard-code observations on August 16–17, 1998. The vignetting is due to overspread aliasing from using the standard-code method.
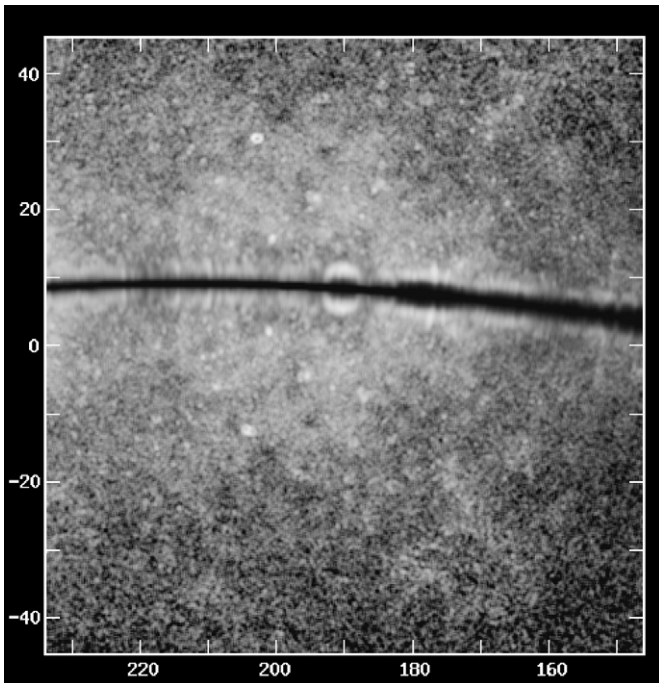

Fig. 20. Arecibo radar image of the circum-Caloris region (SC polarization) from observations on July 15–16, 2005. A 3 × 3-pixel smoothing was applied to reduce noise. σ°_{SC}(max.) = 0.0474.
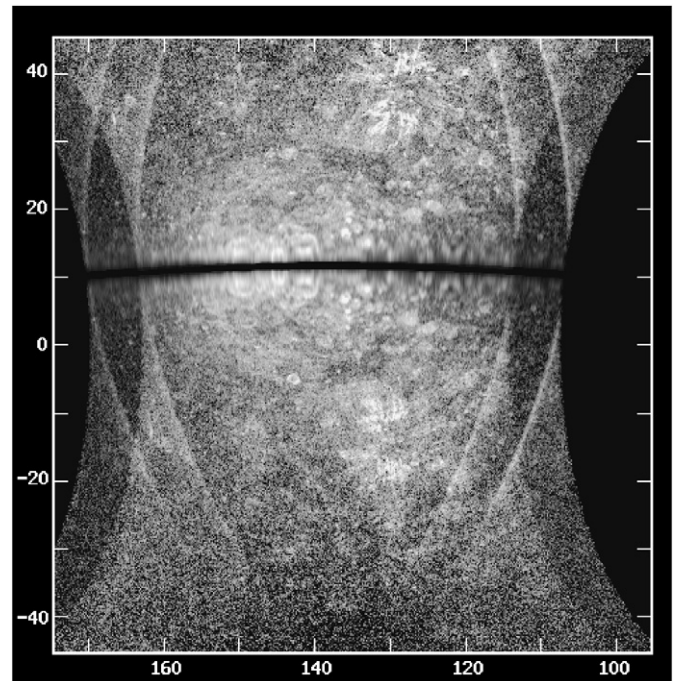

Fig. 22. Arecibo radar image (SC polarization) from standard-code observations on July 25–26, 1999. The vignetting is due to overspread aliasing. The gray scale has been truncated at 0.5 of the maximum brightness.

the NE corner of Fig. 15b and the NW corner of Fig. 19. What radar brightness can be seen from southern Caloris is mostly ambiguity foldover from Tir Planitia (see Section 3.2.2). The only unambiguous radar features from Caloris are a few small to medium-size bright craters, the largest and most prominent being the SC ring feature at 203° W, 30° N (Fig. 12e) and a

105-km-diameter crater at 193° W, 26° N. There are no obvious diffuse SC patches similar to those seen in the circum-Caloris smooth plains, nor is there any obvious SC feature from Caloris Montes. Butler et al. (1993) found a bright OC feature centered on the southeast rim of Caloris in the VLA images. Our OC im-

ages show some modest OC brightness from the Caloris Montes and Mozart ejecta blanket north of Mozart, but no diffuse bright feature from the interior basin floor itself. It should also be noted here that we do not see any obvious SC feature from the "hilly and lineated" terrain at the Caloris antipode (centered near 20° W, 30° S), as can be seen from inspection of the image in Fig. 6.

3.3.2. Circum-Caloris smooth plains

Among the more prominent radar-bright features in Fig. 19 are the two large, diffuse butterfly shaped features folded about the Doppler equator near 150° W and 180° W longitude. Comparison of images taken at different sub-Earth latitudes (Figs. 19–22) indicates that the western feature comes mainly from the south, that is, from the circum-Caloris smooth plains in Tir Planitia, while the eastern feature comes mainly from the Budh Planitia smooth plains north of the Doppler equator. Another large bright patch (surrounding the rayed crater Degas) can be seen in the NE corner of Fig. 19 and the top center of Fig. 22. This feature is associated with the smooth plains in Sobkou Planitia. Finally, in Figs. 19 and 21 can be seen a smaller bright patch (164° W, 16° S) from the smooth-plains floor of Tolstoj Basin.

We show the Tir Planitia region in more detail (and in both polarizations) in Figs. 23 and 24, which are from the same data as in Figs. 19 and 21, respectively. This region is also covered in Fig. 25, which shows the Mariner image mosaic of the H-8 (Tolstoj) quadrangle. The NW corners of the OC images clearly show the smoothness of Tir Planitia, although some confusing foldover can be seen from the northern ejecta of Mozart Crater in the 2002 image (Fig. 23a). The smooth floor of Tolstoj Basin (164° W, 16° S) also shows up nicely in the SE part of Fig. 23a. Note the corner vignetting and horizontal streaking in the lower part of the 1998 OC image (Fig. 24a), which illustrates the effect of Doppler aliasing and code sidelobe leakage in the standard-code observations. The two SC images (Figs. 23b and 24b) clearly show the diffuse brightness from Tir Planitia in their NW quadrants. Both images show a close correspondence between the edge of the radar-bright region and the boundary between the Tir smooth plains and the cratered terrain to the southeast (cf. Fig. 25). Clearly, these smooth plains have a higher depolarized albedo than the adjacent cratered terrain. Portions of Tir Planitia are also bright in the VLA map (Fig. 4), and the implied enhanced depolarized backscatter from smooth plains deposits was recognized and discussed by Butler et al. (1993) and Butler (1994).

The SC feature in Fig. 20 indicates that the Tir Planitia smooth plains continue on west of the 190° W Mariner terminator and well into the MUH. This is also apparent from the VLA image (Figs. 4 and 14) and the "trans-Caloris" Arecibo image (Fig. 15). Extension of the southern circum-Caloris smooth plains into the MUH had also been inferred from the old Arecibo radar altimetry (Harmon et al., 1986; Harmon and Campbell, 1988; Harmon, 1997), which showed smooth downwarped topography along the equator and beyond 210° W that was ascribed to subsidence under the load of the smooth plains fill.
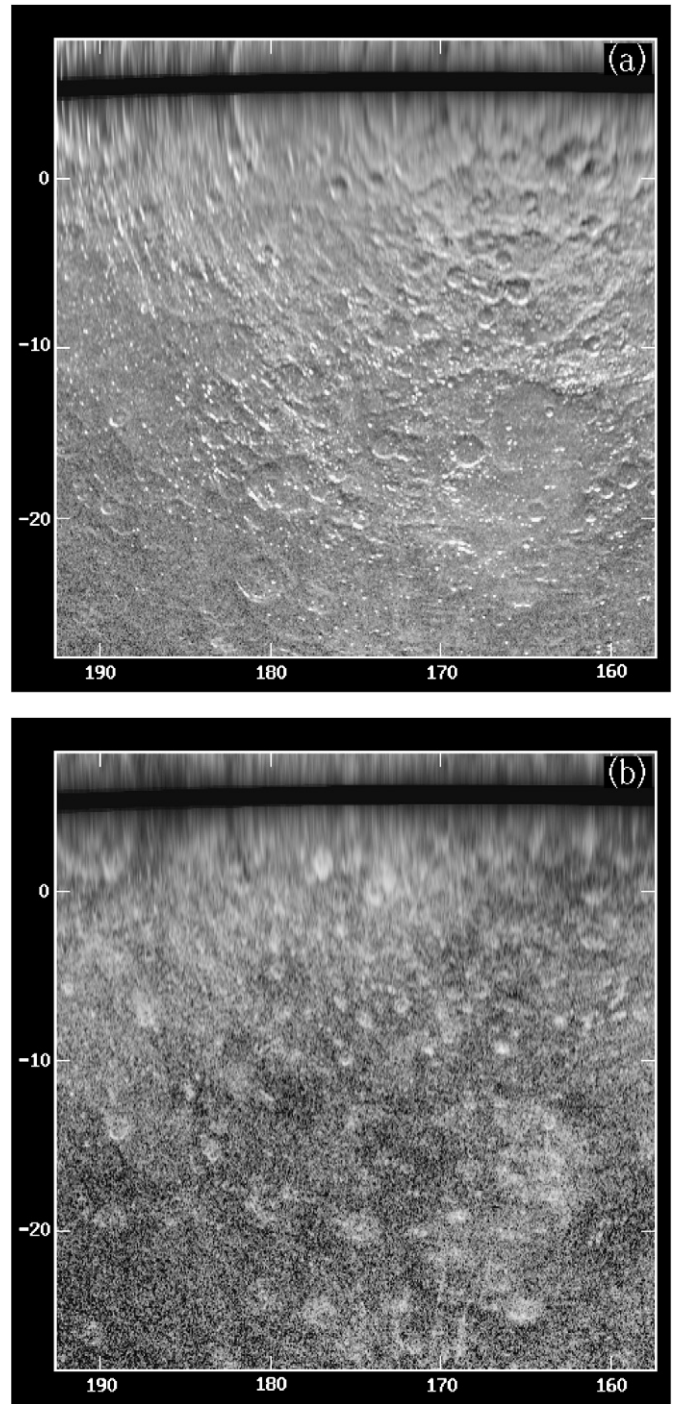

Fig. 23. Arecibo radar images of the Tir–Tolstoj region in (a) OC and (b) SC polarizations. The data are from June 9–10, 2002. Tir Planitia is in the NW quadrant, Tolstoj Basin is in the SE, and Mozart Crater is in the NW corner. σ_{SC}°(max.) = 0.0518.

The large SC bright patch north of the Doppler equator between 145° and 160° W (Figs. 19 and 22) falls within the boundaries of Budh Planitia; this region of Budh northwest of Balzac is also bright in the VLA map (Fig. 4). There is a smaller bright patch in the Arecibo image centered at 139° W, 19° N (just NNE of Harunobu Crater) that coincides with an isolated bay of smooth plains just east of Budh (King and Scott, 1990).
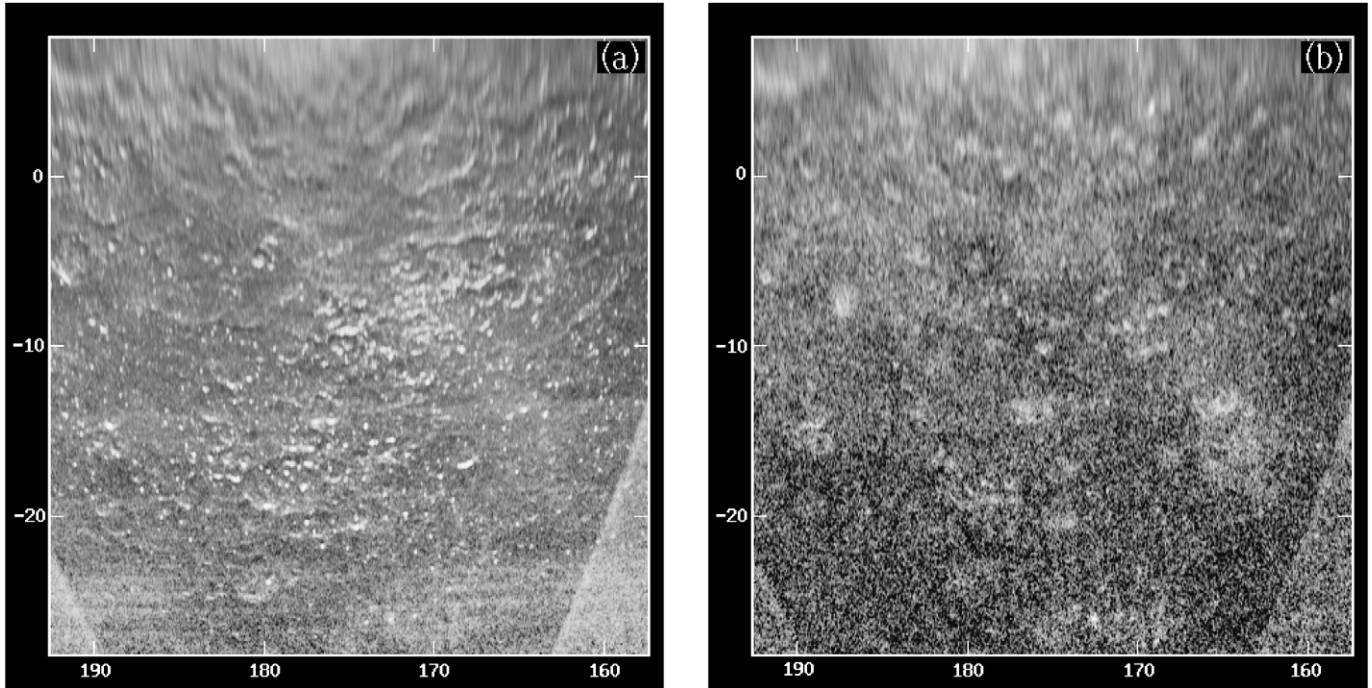
Fig. 24. Arecibo radar images of the Tir–Tolstoj region in (a) OC and (b) SC polarizations. The data are from standard-code observations on August 16–17, 1998. Tir Planitia is in the NW quadrant, Tolstoj Basin is in the SE, and Mozart Crater is in the NW corner. The vignetting at the bottom corners is due to overspread aliasing, while the horizontal streaks in the lower part of the OC image are due to code-sidelobe leakage from using the standard-code method.

To the north of this is a radar-dark region that corresponds to the intercrater plains south of Sobkou Planitia (Guest and Greeley, 1983). The smooth plains of Sobkou Planitia (118°–140° W, 29°–45° N) are radar-bright, showing a well-defined brightness boundary at the contact with the intercrater plains to the south (see the NE corner of Fig. 19 and top of Fig. 22). There is also a corresponding bright patch in the Goldstone-VLA map (Fig. 4), although radar-bright Degas Crater must also be contributing to the X-band feature. The dark SC band west of Budh (at around 160° W, 5° N) corresponds to the Odin Formation (Schaber and McCauley, 1980) separating Budh from Tir Planitia.

In summary, then, there is a clear tendency for the circum-Caloris smooth plains to have higher depolarized brightness than the surrounding intercrater plains. This is an interesting result, in that it is the reverse of the radar brightness contrast seen between the lunar maria and highlands. This point will be treated further in Section 4.

3.3.3. Mozart Crater

One of the more distinctive radar features in the Caloris region (see Figs. 19–24) is the large ring associated with the large c_4-class crater Mozart (190.5° W, 8° N). The dominant ring feature appears to be coming from the interior rim base. In addition, there is a hint of a faint inner ring (see Fig. 19), which is consistent with the identification of Mozart as a two-ring basin by Pike (1988). Beyond the outer ring is a radar-dark halo that includes the rim and the surrounding ejecta blanket. It is important to note that the wide bright SC halo beyond Mozart's dark ejecta halo is not associated with Mozart, but rather is the enhanced depolarized backscatter from Tir Planitia upon which Mozart and its ejecta are superimposed.

3.3.4. Tolstoj–Zeami–Balzac region

Here we discuss the interesting and varied region south of Tir/Budh Planitiae. This region is covered in Fig. 26, which shows Arecibo OC/SC images from 2002 June 9–10 plus smaller insert images from 1999 July 25–26 that span part of the corrupted Doppler equator region of the 2002 images. Largely covered by intercrater plains, the region includes Tolstoj Basin in the southwest, a collection of prominent fresh craters (Zeami, Balzac, etc.) in the east, and the grooved and lineated terrain in the Goya region NE of Tolstoj (see Fig. 25). Tolstoj Basin is also visible in the SE corner of Fig. 23.

Figs. 23a and 26a clearly show the smooth floor of Tolstoj Basin, while the corresponding SC images in Figs. 23b and 26b show the bright depolarized feature coming from the basin interior and centered near 164° W, 16° S. (The fact that the SC feature is seen in the same location in Fig. 24b confirms Tolstoj as the source.) The H-8 geologic map (Schaber and McCauley, 1980) assigns the basin interior the same "smooth plains" designation as the circum-Caloris plains, making this yet another example of a smooth-plains region showing high depolarized brightness relative to the intercrater plains. However, not all of the Tolstoj smooth plains exhibit this radar brightness. Also, there is no obvious bright feature from Tolstoj in the VLA map (Fig. 4), and the basin appears dark in telescopic images (Warell and Limaye, 2001; Mendillo et al., 2001).

The region immediately NE of Tolstoj shows considerable topographic detail in the OC image, but little in the way of depolarized structure. The OC image (Fig. 26a) clearly shows the topographic groove starting at the north rim of Rublev Crater (157.5° W, 14.5° S) and extending NE toward the south rim of Zeami Crater (148° W, 2.5° S) (see also Fig. 25). This is
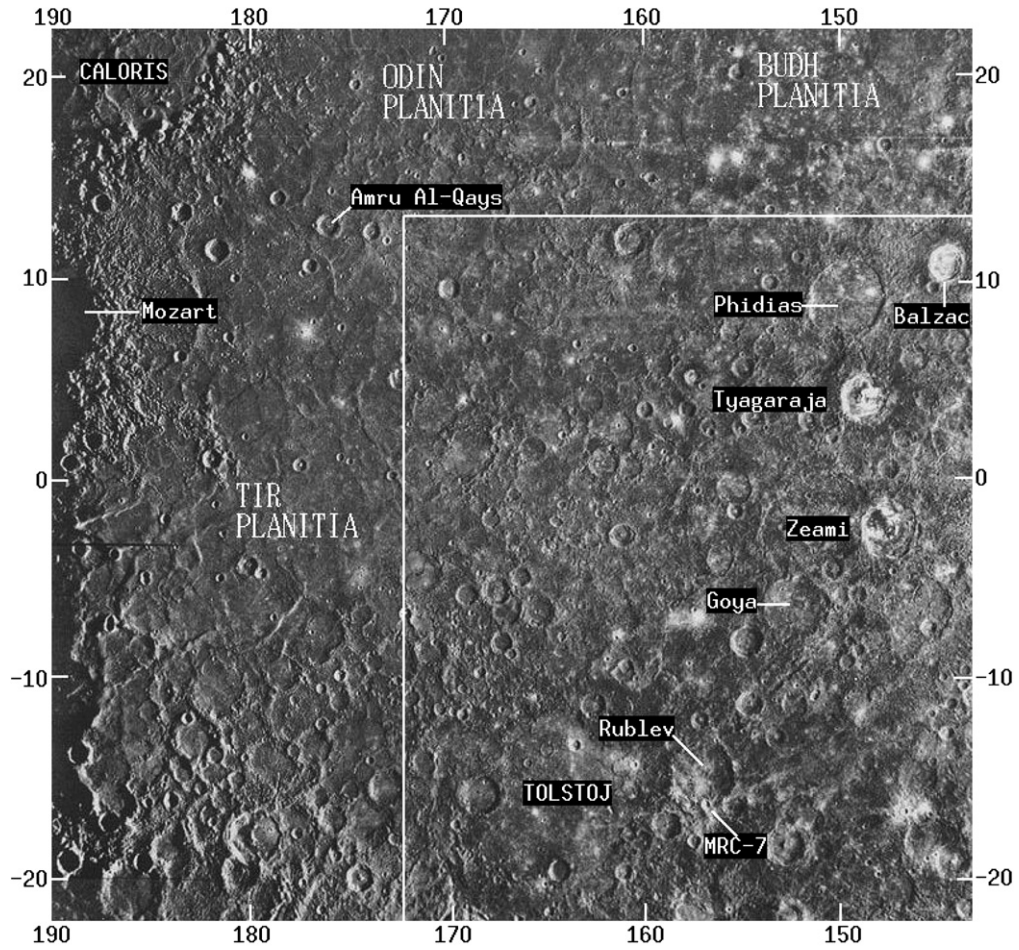
Fig. 25. Mariner 10 image mosaic of the H-8 (Tolstoj) quadrangle of Mercury, with labels denoting features referred to in the text. The box shows the north and west boundaries of the images in Fig. 26. The Mariner departure terminator is the dark edge on the left. Adapted from the Atlas of Mercury (Davies et al., 1978).
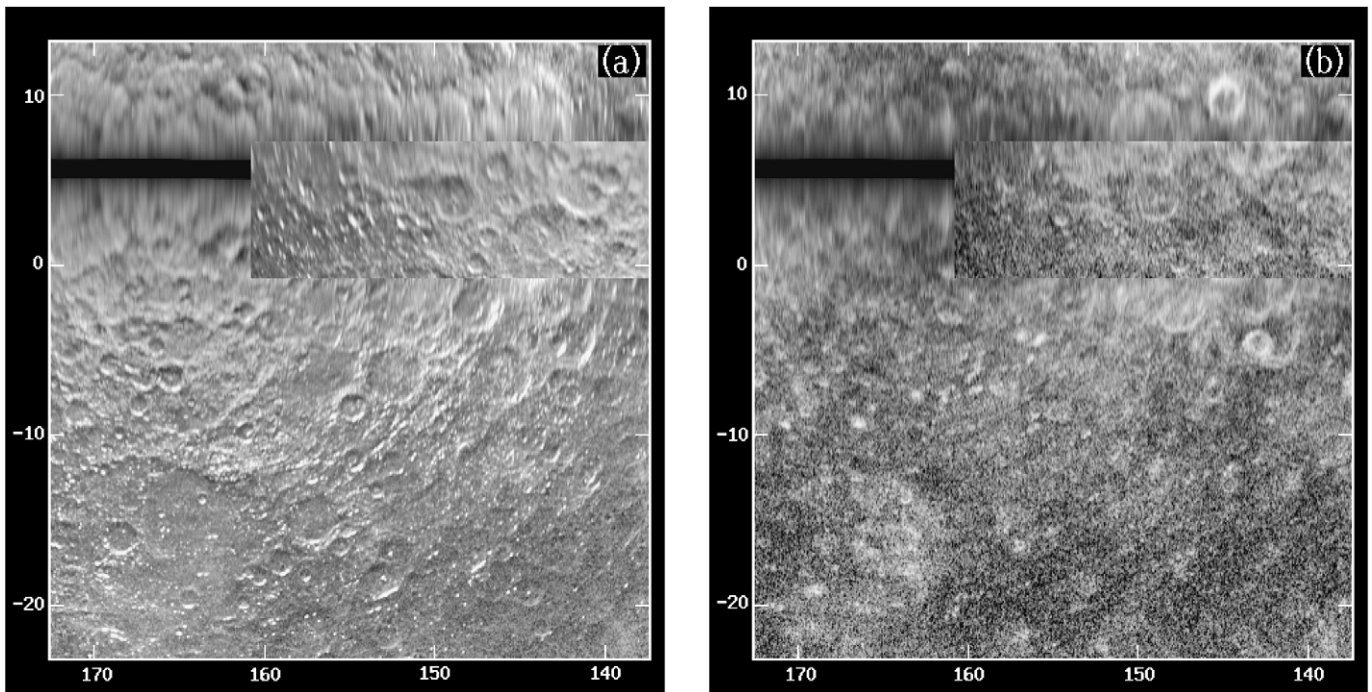

Fig. 26. Arecibo radar images of the Tolstoj–Zeami–Balzac region in (a) OC and (b) SC polarizations. The data are from June 9–10, 2002, with an additional image insert from July 25–26, 1999. $\sigma_{\text{SC}}^{\circ}(\text{max.}) = 0.0552$.

the most prominent of several grooves that Thomas (1997) has suggested are graben produced in a post-Tolstoj tectonic uplift. None of the lineaments or craters in this region between Tolstoj and Zeami show much SC structure, and the moderately enhanced SC brightness background of the region is mostly attributable to N/S-ambiguity foldover from Budh Planitia. It is also interesting to note that two prominent bright spots in the Mariner images, at 157° W, 7° S and 158° W, 3° N, show no corresponding radar bright spots; this is in contrast to similar bright spots in the smooth plains to the north (Section 3.3.6) that do show radar-bright spots. The fresh-appearing (c_5-class) craters Zeami (148° W, 2.5° S) and Tyagaraja (149° W, 4° N) show only narrow SC features from their south rims that are no more prominent than the rim feature from the degraded (c_2-class) crater Phidias (149.5° W, 9° N). The smaller c_5-class crater Balzac (145° W, 10° N), on the other hand, shows a prominent bright rim ring. The Balzac region is also bright on the VLA map (Fig. 4). The one other crater showing a very bright rim ring is Theophanes (143° W, 4° S), located just beyond the eastern boundary of the H-8 quadrangle. This 50-km-diameter crater, which shows a very bright floor but only a single, faint ray in the Mariner images (see Section 3.4), has been mapped as c_4-class in the H-7 geologic map of King and Scott (1990). A detail image pair for Theophanes is shown in Fig. 12f.

3.3.5. Rayed craters: Bashō, Degas, MRC-7

Craters Bashō (170.5° W, 32° S) and Degas (127° W, 37.5° N) are two of the most prominent crater features in the large-scale SC image of the region (Fig. 19). They are also among the most prominent of the rayed craters seen by Mariner 10 (Fig. 3), with Degas being particularly striking. Both craters are classified as c_5 in the USGS geologic maps of the H-12 (Spudis and Prosser, 1984) and H-3 (Guest and Greeley, 1983) quadrangles. The Mariner image mosaics of these two quadrangles are shown in Figs. 27 and 28. Closeup OC/SC image pairs of Bashō and Degas are shown in Figs. 29 and 30, respectively. Although the two craters have rather different sizes (70 and 45 km) and optical appearances (Bashō's ejecta blanket shows a dark halo, while Degas's is mostly bright), their radar appearances are very similar. Both show irregular ray haloes that are offset from the crater by about five crater radii. Both also show a bright crater floor rather than the dark floor and bright rim collar seen with other fresh craters. All of Degas's radar rays coincide with optical rays, although the converse is not the case. A portion of the long optical ray extending ESE of Degas can be seen in the SC image. Bashō's optical rays stand out less than Degas's, possibly owing to lower sun angles, and some of the radar rays are difficult to make out in the Mariner images. One very long radar ray can be seen extending west of Bashō to 197° W longitude (Fig. 19).

Visible in Fig. 30a is a bright streak running diagonally through the center of the image and east of Degas. This same feature can be seen in the Mariner images (Fig. 28) and also appears in the sketch map in Fig. 3. This feature may be a ray from a small rayed crater located southwest of Gauguin Crater at 102° W, 65° N, although it would be remarkable for such a large ray to emanate from such a small crater. Also unusual is the fact that the radar ray shows up best in the OC polarization.

One other Mariner rayed crater (MRC-7) can be seen in the radar images (Fig. 26) as the small crater on the south rim of Rublev Crater. The Mariner images (Fig. 25) show a bright crater and halo, along with rays extending to the east and west. The SC radar image shows a bright rim ring and a faint narrow ray coinciding with the optical ray extending to the ENE. A closeup image of this crater is shown in Fig. 12g.

3.3.6. Other bright craters and clusters

Numerous bright SC crater features have been found in this region, in addition to those already discussed in the two previous sections. The smallest craters tend to be distributed in loose clusters north of the Doppler equator in Fig. 19. One of these clusters is located southwest of Van Eyck basin in terrain mapped mainly as Odin Formation (Guest and Greeley, 1983). The location of this cluster in the Mariner images is shown in Fig. 28, and the corresponding SC radar image of the cluster is shown in Fig. 31. This image is dominated by a bright ring feature from a 40-km-diameter crater at 164.5° W, 36.5° N. An OC/SC image pair for this crater is also shown in Fig. 12h. The bright rim collar starts at the crater's inner rim base and extends one crater radius beyond the rim. South and west of this crater are numerous smaller crater spots, many of which are also resolved into rim rings. The smaller of these craters are about 5 km in size, and some of these show bright haloes in the Mariner images. The brightest spot in the Mariner image of the region (see Fig. 28) lies beyond the east edge of Fig. 31 at 152.5° W, 36° N, and our SC images (Figs. 19, 21, 22) show a corresponding bright radar spot.

Another loose clustering of small bright SC features can be seen extending from Budh Planitia at around 15° N to Odin Planitia at around 20° N. Several of these coincide with small bright-halo craters or other bright spots in the Mariner images. Of particular interest is a pair of bright spots located in the Budh smooth plains near 156° W, 16° N. These can be seen in the large-scale SC images (Figs. 19–22) and in foldover (at 4° S Lat.) in Fig. 26. These are prominent in the Mariner images (Fig. 25) and have a very similar (non-ring) appearance in the SC radar images. Although both of these spots are represented as small craters on the shaded relief maps in the *Atlas of Mercury* (Davies et al., 1978), they do not show any obvious crater structure in the OC and SC radar images or in the Mariner images. They are similar in optical appearance to the two bright spots that were seen in the Mariner images farther south in the intercrater plains at 157° W, 7° S and 158° W, 3° N (see Section 3.3.3), although the latter did not show up as SC radar bright spots. This result, and the possibility that smooth plains in general tend to better preserve their radar-fresh crater features, will be discussed later.

Farther south in Tir Planitia, and just north of the Doppler equator in Fig. 19, are some bright crater features in the vicinity of Amru Al-Qays Crater. The c_4-class Amru Al-Qays (176° W, 12.5° N) itself shows no bright SC feature, whereas the c_3-class crater (176.5° W, 10.5° N) just to its SSW does. The
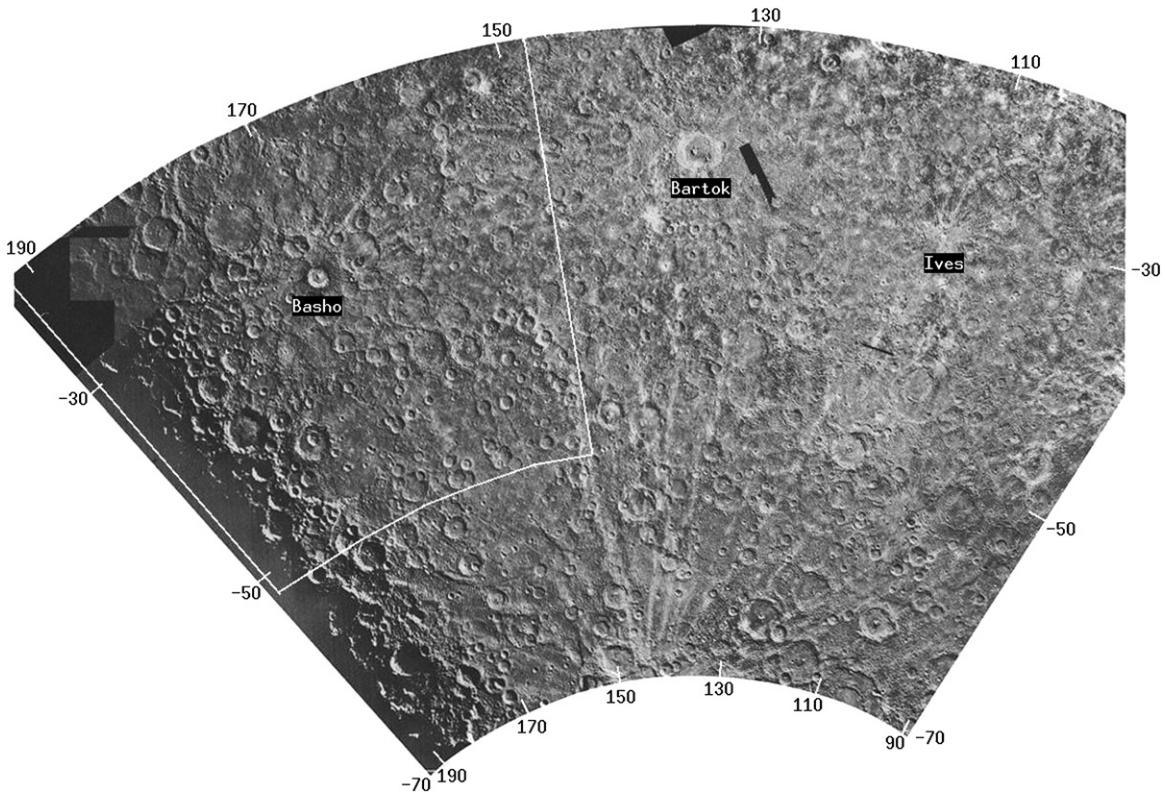
Fig. 27. Mariner 10 image mosaic of the H-12 (Michelangelo) quadrangle of Mercury, with labels denoting craters referred to in the text and a box showing the south, east, and west boundaries of the images in Fig. 29. The Mariner departure terminator is the dark edge on the left. Adapted from the Atlas of Mercury (Davies et al., 1978).
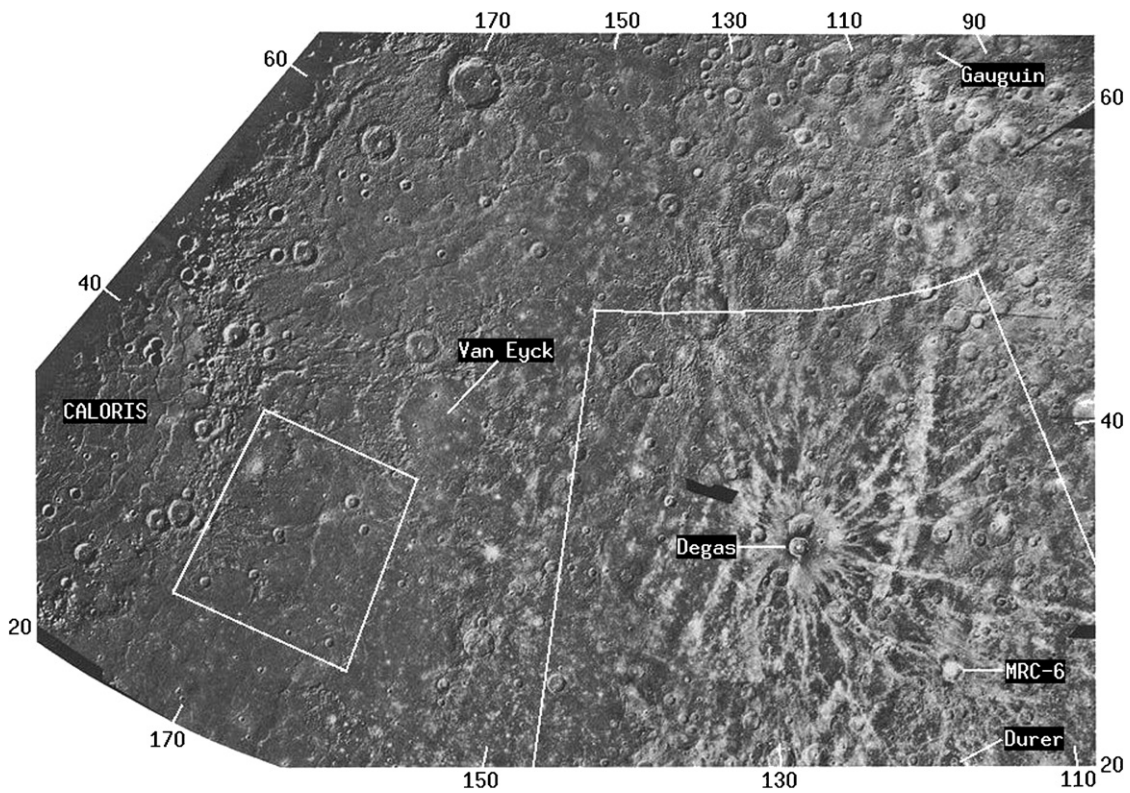

Fig. 28. Mariner 10 image mosaic of the H-3 (Shakespeare) quadrangle of Mercury, with labels denoting craters referred to in the text. The box at right shows the north, east, and west boundaries of the images in Fig. 30. The box at left shows the boundaries of the image in Fig. 31. Adapted from the Atlas of Mercury (Davies et al., 1978).
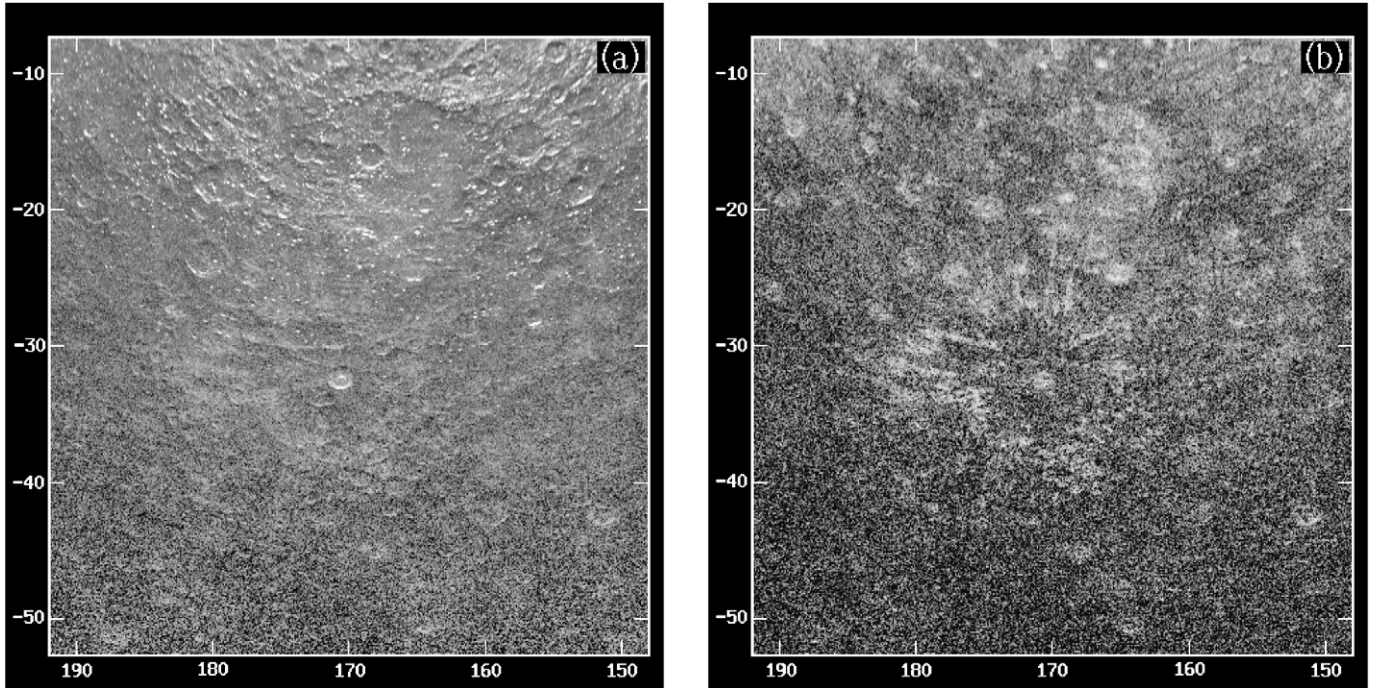
Fig. 29. Arecibo radar images of Bashō Crater and environs in (a) OC and (b) SC polarizations. The data are from June 9–10, 2002. Bashō Crater is at center and Tolstoj Basin is visible at top. $\sigma^\circ_{sc}(\text{max.}) = 0.0512$.
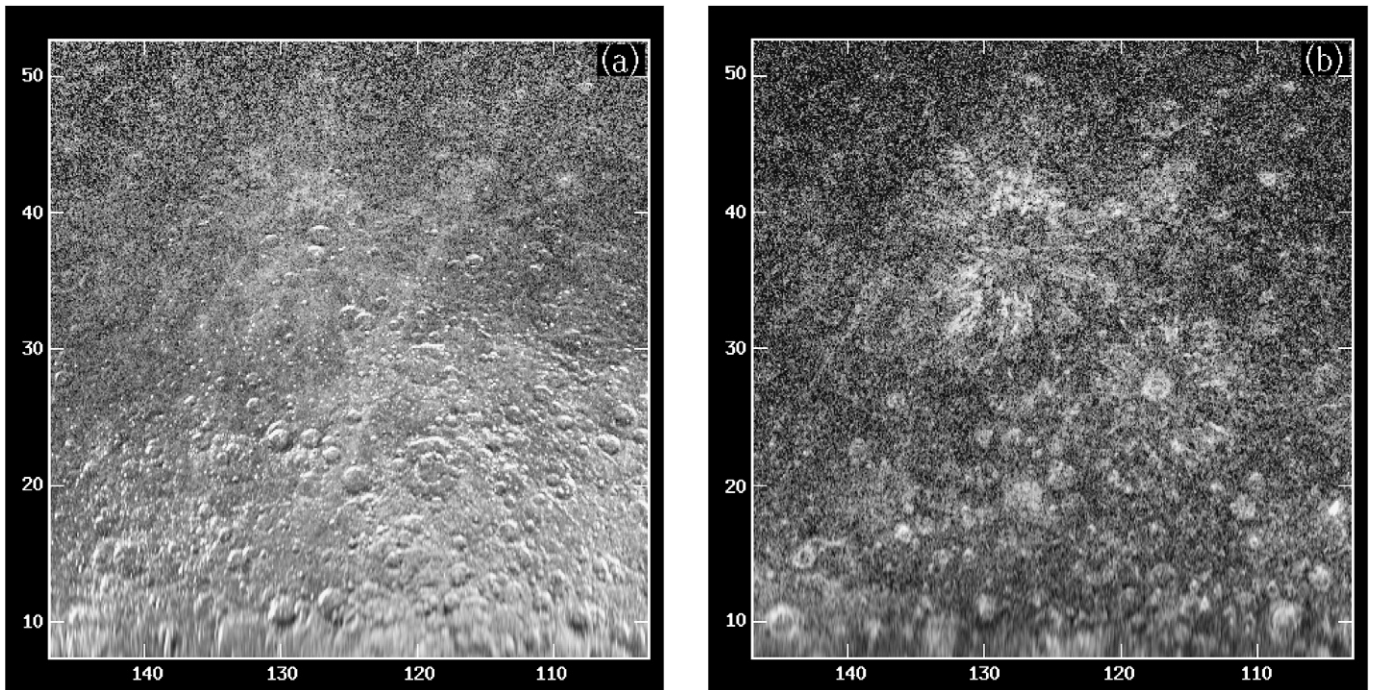

Fig. 30. Arecibo radar images of Degas Crater and environs in (a) OC and (b) SC polarizations. The data are from June 2, 2002. Degas Crater is just north of center. Southeast of Degas are the rayed crater "MRC-6" and the two-ring basin Dürer. The gray scale of the SC image has been truncated at 0.3 of the maximum brightness. $\sigma^\circ_{sc}(\text{max.}) = 0.275$.

c_5 crater (174° W, 12.5° N) just east of Amru Al-Qays also shows a bright rim, while an even brighter feature comes from the smaller crater just beyond this crater's southeast rim. This smaller crater (173.2° W, 12° N) is unclassified in the geologic map of Schaber and McCauley (1980), but shows a bright halo and rays in the Mariner images. It has even been claimed as

the possible source of a bright telescopic feature (Warell and Limaye, 2001).

Farther south and west in Tir are several other radar-bright craters. One of these is a c_4-class crater located at 189° W, 14° S, while another is an irregular or double crater at 187.5° W, 7° S. To the ENE at 180° W, 4.5° S is a c_4 crater with a mod-

est bright rim surrounded by a large dark halo. Apparently, the fresh ejecta from this crater are obscuring the brighter smooth plains that they overlay. In the intercrater plains due south of this crater we see rim and central-peak features from the

large c_4 crater Kalidasa (180° W, 18° S) and from the smaller c_5 crater (174.8° W, 19.5° S) just to the ESE.

3.4. Central MIH region

In this section, we survey most of the radar features seen east of Theophanes and west of Kuiper (the exception being Degas Crater, which was treated in the last section). The equatorial portion of this region includes all of the USGS H-7 quadrangle and the western part of the H-6 quadrangle. Except for a few data gaps or "gores," this entire region is covered by Mariner images. In Fig. 32 we show the Mariner image mosaic of the H-7 (Beethoven) quadrangle. As can be seen from this mosaic, the Mariner image quality over most of the H-7 quadrangle is relatively poor owing to high Sun angles. Such high illumination does not produce the shadowing that brings out large-scale relief, although it will tend to accentuate optical albedo features. The Mariner images of H-7 do, in fact, show the richest albedo structure on the planet (mostly bright craters and rays). One of the purposes of the Arecibo radar imaging was to determine if this was simply an artifact of the high sun angles or a real indicator of a high density of fresh impacts. Fortunately, we have obtained good Arecibo imaging over the region from observations made at the minimum Earth–Mercury distance. The sub-Earth longitudes of the Goldstone-VLA observations were not favorable for X-band radar imaging of the region, although some features were visible toward the disk limbs and are mapped in Fig. 4.

Large-scale Arecibo SC images of the region are shown in Figs. 33–35. Fig. 33 shows an image of the western side of the region from data taken on June 2, 2002. Regions farther to the east are covered by the SC images in Fig. 34 (from June 13,
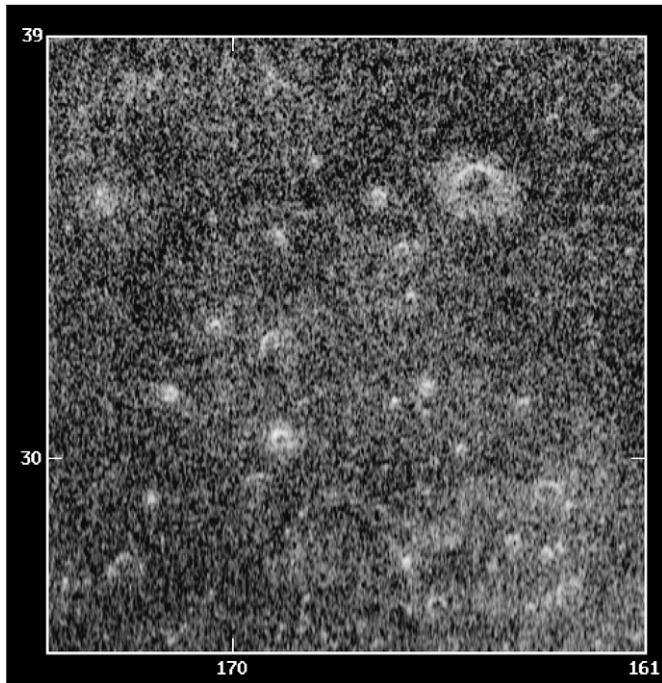
Fig. 31. Arecibo radar image (SC polarization) of the bright crater cluster between Odin Planitia and Van Eyck Basin. The data are from June 9–10, 2002. The largest crater (upper right) is the same crater shown in Fig. 12h. $\sigma_{sc}^\circ (\text{max.}) = 0.0963$.
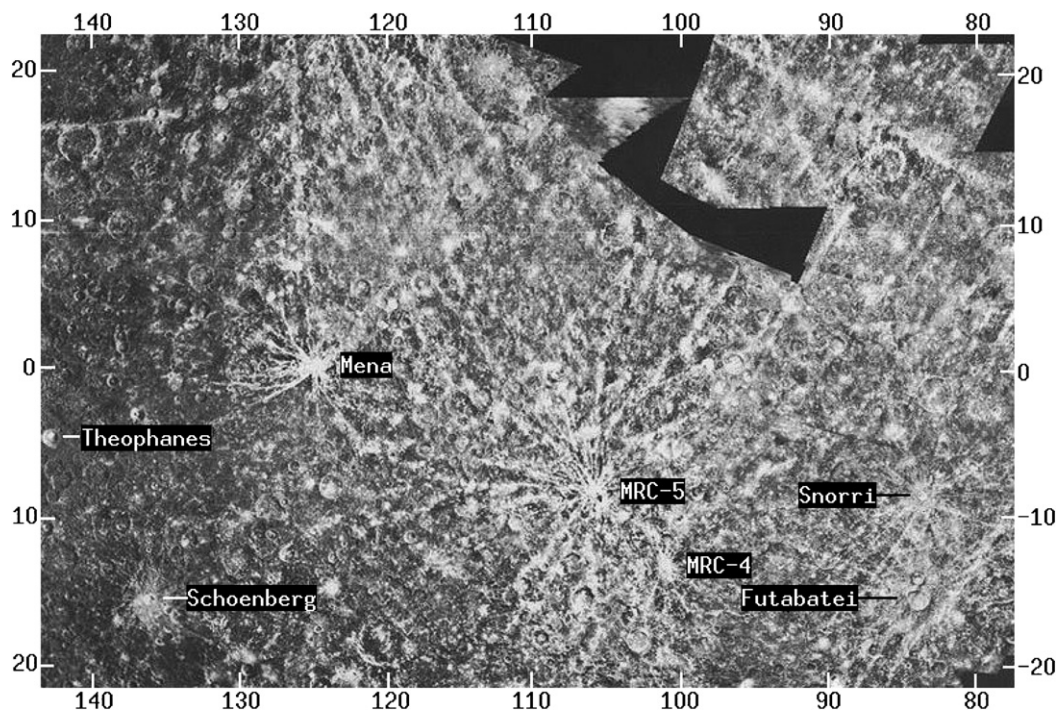
Fig. 32. Mariner 10 image mosaic of the H-7 (Beethoven) quadrangle of Mercury, with labels denoting craters referred to in the text. Adapted from the Atlas of Mercury (Davies et al., 1978).
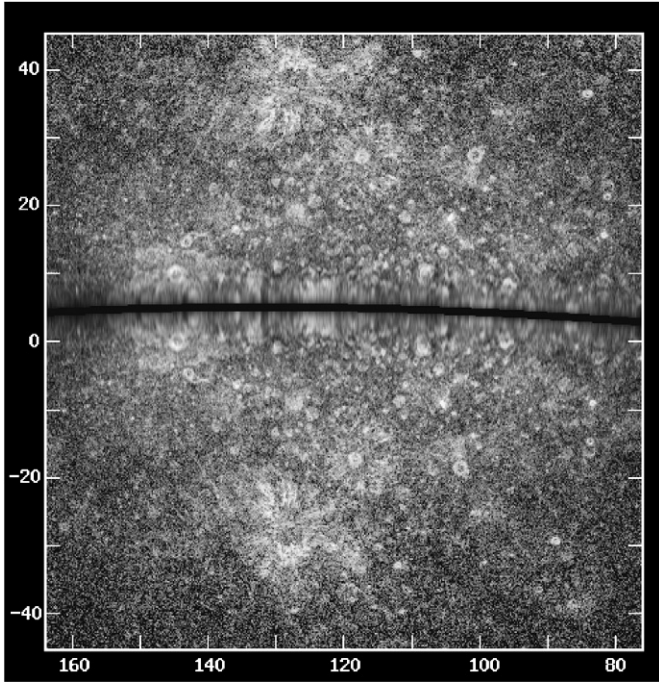
Fig. 33. Arecibo radar image (SC polarization) of the "central MIH" region. The data are from June 2, 2002. The gray scale has been truncated at 0.3 of the maximum brightness. $\sigma_{SC}^{\circ}(\text{max.}) = 0.218$.
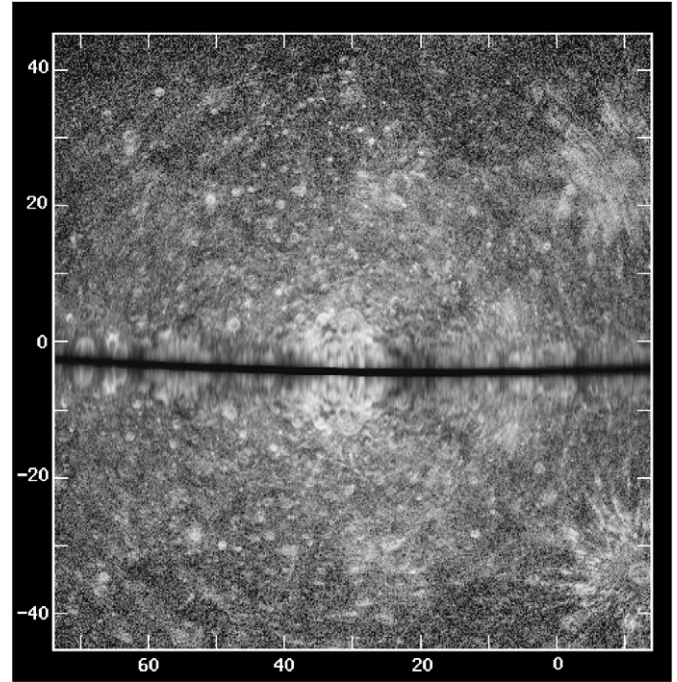

Fig. 35. Arecibo radar image (SC polarization) of an eastern portion of the MIH region. The data are from April 14–17, 2004. $\sigma_{SC}^{\circ}(\text{max.}) = 0.0578$.
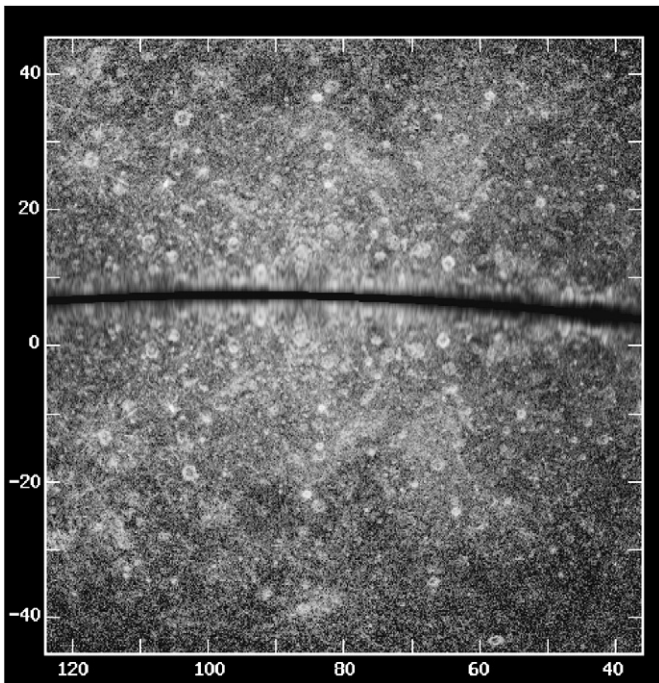

Fig. 34. Arecibo radar image (SC polarization) of the "central MIH" region. The data are from June 13, 2001. The gray scale has been truncated at 0.3 of the maximum brightness. $\sigma_{SC}^{\circ}(\text{max.}) = 0.211$.

2001) and Fig. 35 (from April 14–17, 2004). These SC images show a plethora of bright crater features over the H-7 quadrangle and into the western end of H-6, which suggests that the apparent abundance of fresh craters in this region is real. These features are discussed in more detail in the following two subsections.

3.4.1. Mariner rayed craters

Nearly all of the "Mariner rayed craters" shown in Fig. 3 and listed in Table 2 show some sort of radar-bright feature. However, only one, MRC-6 (117.2° W, 27.6° N), shows extended ejecta and rays to radar. This crater can be seen to the southeast of Degas and NNE of Dürer in Fig. 30; it can also be seen in the upper center of Fig. 33 and NW corner of Fig. 34. This crater is about the same size as Degas and shows a similar, but fainter, radar ray/ejecta pattern. Unlike Degas, it shows a bright rim ring. The crater is classified as c_4 in the H-3 geologic map (Guest and Greeley, 1983). To the south of MRC-6 and Dürer is the small rayed crater Mena (125° W, 0.1° N). Mena is the only "Mariner rayed crater" that does not show a radar bright feature, which is curious given its prominence in the Mariner images (see Fig. 25) and its optical similarity to other small rayed craters that do show radar features. In fact, the rayed crater that most closely resembles Mena optically, MRC-5 (105.7° W, 8.5° S), shows the brightest depolarized feature on the planet (aside from the polar ice features). This crater, which is shown in closeup in Fig. 12i, shows a bright rim ring as well as a curious bright ejecta wedge or spray that extends a short distance to the SSE. This feature has a peak SC brightness $\sigma_{sc}^{\circ} = 0.290$, or more than 50 times the disk averaged SC albedo of the planet and about three times the typical maximum brightness of other radar-bright craters. The extreme radar brightness of this feature, and the very prominent optical ray system, suggests that this may be the freshest small impact crater on Mercury or that the ejecta structure is unusually conducive to strong volume scattering and/or coherent backscatter. This feature is so bright that the large-scale SC images of the region (Figs. 33 and 34) had to have a gray-scale

truncation of 0.3 to reduce their dynamic range. Not surprisingly, it appears to be the source of a bright spot in telescopic images (Warell and Limaye, 2001). To the SE is the less impressive rayed crater MRC-4 (101° W, 13.2° S), which is shown in closeup in Fig. 12j. The SC signature of this crater is the more familiar bright rim ring. Two other prominent Mariner rayed craters in the region showing radar-bright floors and rims, but no radar rays, are Ives (112° W, 32.5° S) and Schoenberg (136° W, 15.5° S) (Fig. 33).

Farther to the east are seen bright features from several other Mariner rayed craters. Crater Snorri (83.5° W, 8.5° S) is yet another prominent rayed crater showing a radar-bright rim ring but no radar rays (Fig. 12k). Due south of Snorri is Futabatei Crater (83.5° W, 15.5° S), which does not appear in Fig. 3 or Table 2 but which nevertheless shows prominent ejecta and rays in the Mariner images (Fig. 32). Futabatei itself shows only a faint partial rim ring, while its smaller companion crater just to the north shows a prominent rim ring. (Both craters are shown in Fig. 12l.) This companion crater is interesting in that the bright SC rim ring corresponds to a dark optical halo in the Mariner images. Other Mariner rayed craters showing bright rim rings are Tansen (72° W, 4° N), Copley (86° W, 38° S), a c_5 crater (67° W, 34.5° S) just WNW of Chekhov, MRC-3 (64.8° W, 1.2° N), MRC-2 (50.3° W, 21.5° N), and MRC-1 (49.5° W, 29° S); the last three of these are shown in closeup in Figs. 12m–12o. Craters MRC-2 and MRC-1 also show some SC radar brightness in their central floors. Copley Crater shows an SC feature in the VLA images (Fig. 4), while both Chekhov-WNW and MRC-1 appear to be the sources of bright spots in telescopic images (Warell and Limaye, 2001).

3.4.2. Bartok Crater

There is a very faint feature at the bottom of Fig. 22 associated with the 80-km-diameter crater Bartok (135° W, 29° S). This c_5-class crater shows rays and a very bright rim ring and halo in the Mariner images (Fig. 27). In radar it appears very similar to (if even fainter than) the "ghost feature" discussed in Section 3.2.2, with a bright rim collar, surrounding dark halo, and a dense filigree of outer rays. Western and southern portions of this feature can be seen in Fig. 33 (the remainder being obscured by foldover from Sobkou Planitia and Degas). Long, narrow rays can be seen extending NNW and SSE of Bartok. These rays can also be seen in foldover at the top and left edge of Fig. 30b.

3.4.3. Other craters and basins

There are a number of other craters in this region that show radar-bright features. Among the more prominent of these is an unnamed crater at 102.5° W, 19° S. This crater shows a prominent rim ring (Fig. 12p) and very faint rays in the SC radar images, and also shows an SC feature in the VLA images (Fig. 4). The Mariner images show only a moderately bright floor with no obvious rays or ejecta, and the crater is only classified as c_3 freshness in the H-7 geologic map (King and Scott, 1990). Several other craters can be seen that show radar-bright floors but radar-dark rims; these include Thakur (64° W, 3° S),

Polygnotus (69° W, 0.5° S), Philoxenus (112° W, 9° S), a crater (75° W, 1.5° N) just NW of Boethius, a crater (129.5° W, 0.5° S) just ESE of Lysippus, and a crater at 128° W, 9.5° S. The rims of these craters are all classified c_3 or older, although the floors of several of them are designated "smooth plains" and one, Polygnotus, contains a c_5 core in the central floor. One of them, the crater NW of Boethius, shows a prominent radar-dark halo. Finally, to the north in the H-2 quadrangle are two bright-ring craters at 59° W, 37° N and 84° W, 37° N. Both of these are in or near Mariner coverage gaps, making the identification of their source craters impossible.

The region contains several two-ring basins, only two of which show much in the radar images. Dürer (119° W, 22° N) shows up nicely in the OC (see Fig. 30a), but in the SC only shows some patchy brightness in its outer ring floor. The smaller basin Boethius (74° W, 0.5° S) shows more uniform (though moderate) brightness over the entire floor.

There are also several large basins of note in the region. One of these, Raphael (76° W, 20° S), is uniformly dark in both SC and OC. The very large basin roughly centered on Lysippus (133° W, 1.5° N) is also mostly radar dark, except where there are superimposed craters. It is difficult to evaluate the radar appearance of Beethoven Basin because of confusing foldover from Degas and MRC-6.

3.5. Central MUH region

Here we survey the one remaining region, which covers the MUH between the "Mariner-approach region" (Section 3.1) and the "trans-Caloris region" (Section 3.2), or roughly the longitude span 270–340° W. The VLA images (Fig. 4) do not show any major bright features for the region, and the Arecibo imaging confirms this. Large-scale Arecibo OC/SC images of the region are shown in Figs. 36–38. This includes two images of the western zone (at two different sub-Earth latitudes) from data taken on May 6–7, 2002 (Fig. 36) and August 19, 2004 (Fig. 37), and an image of the eastern zone from August 14–15, 2004 (Fig. 38).

3.5.1. Bright craters

Much of the region is heavily cratered and has a fairly large population of radar-bright craters of various sizes. Two of the more prominent bright crater features are located just north of the equator on the west side of Fig. 36b. One of these, the small bright spot at 339° W, 12° N, corresponds to the 12-km-diameter rim-ring crater already mentioned in Section 3.1.5 (see also Fig. 12b). Just to the ESE lies a much larger feature centered at 327° W, 8° N. A closeup image of this feature is shown in Fig. 39. The feature consists of a 68-km-diameter central crater and a surrounding halo of rays and ejecta. Note that a larger (112-km-diameter) crater is superimposed on the eastern part of the ejecta ring. The most prominent rays extend southwest of the crater. This feature bears some resemblance to the craters Bashō, Degas, and MRC-6. The feature can be seen in the Goldstone-VLA image in Fig. 5, where it is just SE of the brighter spot from the crater at 339° W, 12° N. This feature coincides with a prominent bright
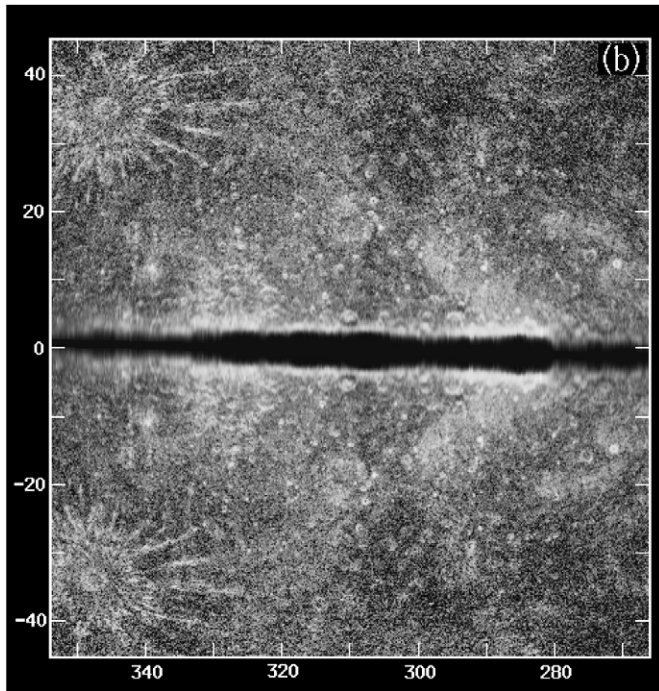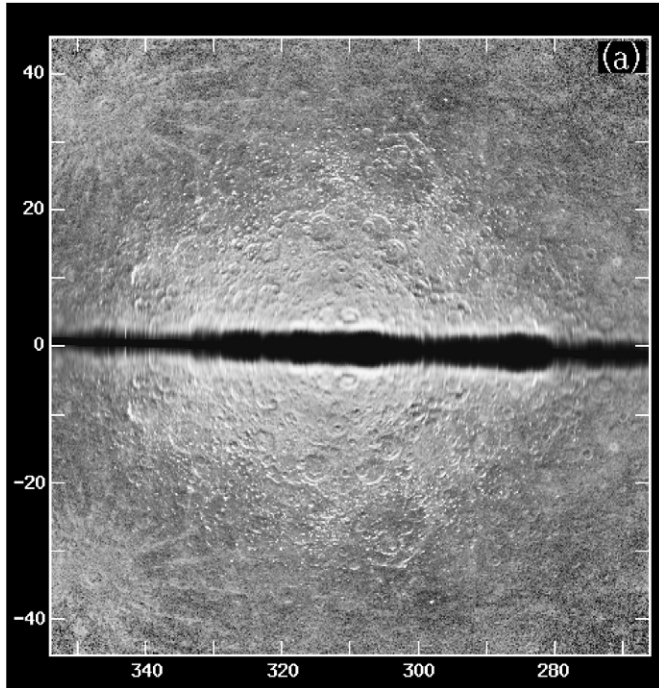
Fig. 36. Arecibo radar images of the "central MUH" region in (a) OC and (b) SC polarizations. The data are from May 6–7, 2002. $\sigma_{SC}^\circ(\text{max.}) = 0.0784$.

Fig. 37. Arecibo radar images of the "central MUH" region in (a) OC and (b) SC polarizations. The data are from August 19, 2004. The gray scale of the SC image has been truncated at 0.5 of the maximum brightness. $\sigma_{SC}^\circ(\text{max.}) = 0.0675$.

spot in optical telescopic images (Baumgardner et al., 2000; Warell and Limaye, 2001), so it is likely to have a bright optical ray system.

Prominent on the western side of Fig. 37 is a dark-halo feature associated with a large (190-km-diameter) crater at 340° W, 9° S. (The SC halo feature does not show as clearly in Fig. 36 owing to foldover from the crater at 339° W, 12° N.) This is probably the most prominent dark-halo crater on the planet.

Numerous other bright crater features can be seen, many of which show the typical rim-ring morphology. Two of the more prominent of these are located farther east at 284° W, 3° S and 272° W, 14° S. Closeup images of these are shown in Figs. 12q and 12r, respectively. The first of these has a narrow ring that hugs the rim, while the second, smaller crater shows an ejecta ring that extends more than one crater radius beyond the rim. A cluster of small bright craters near
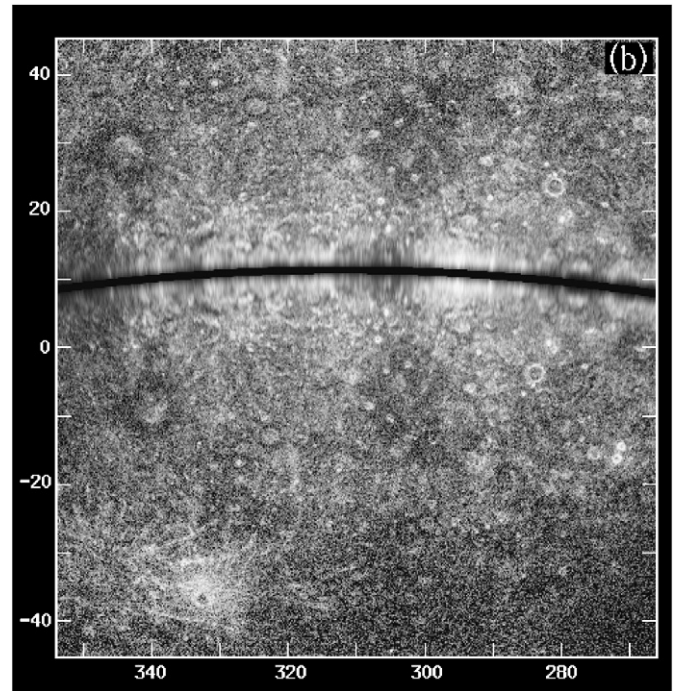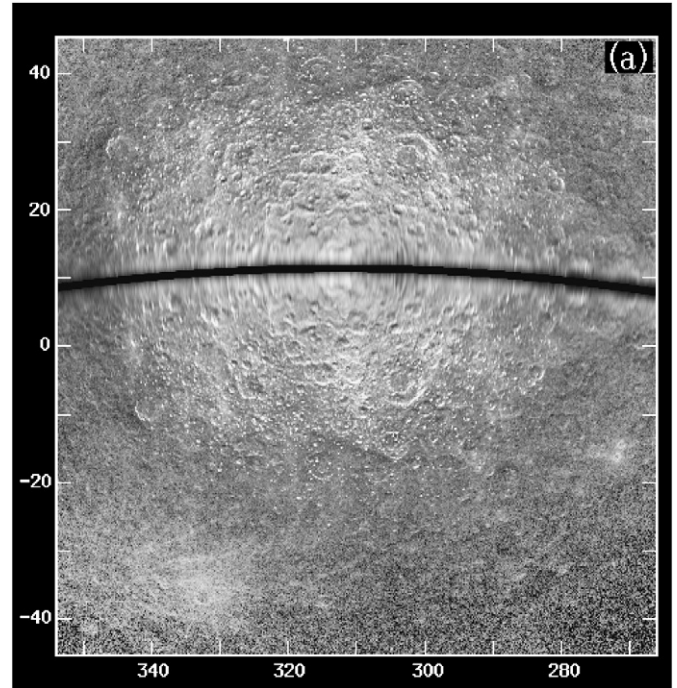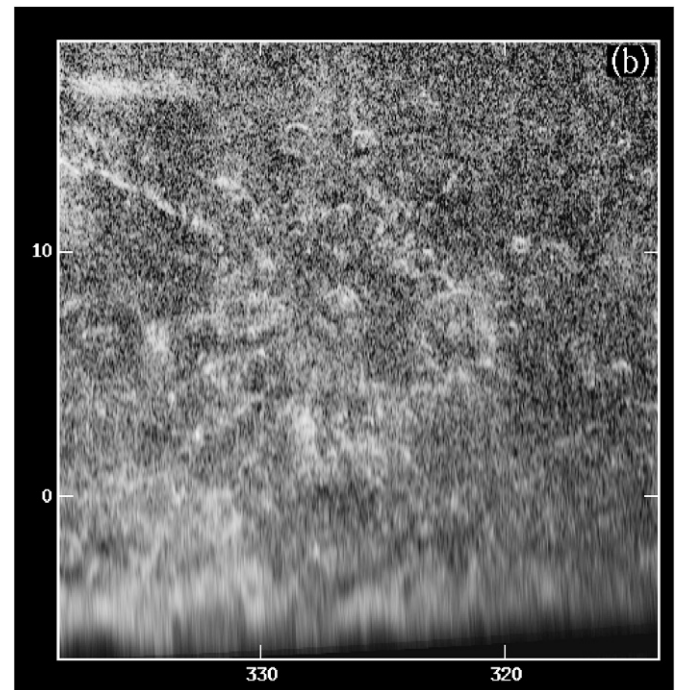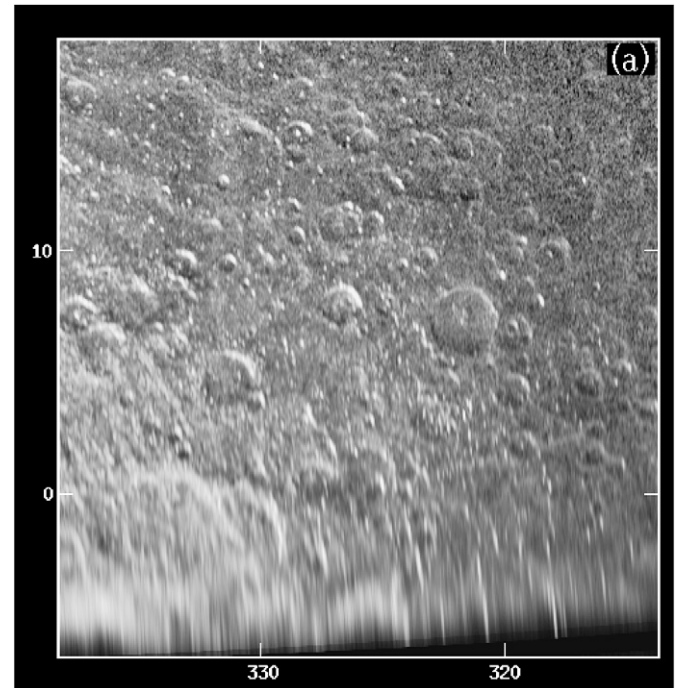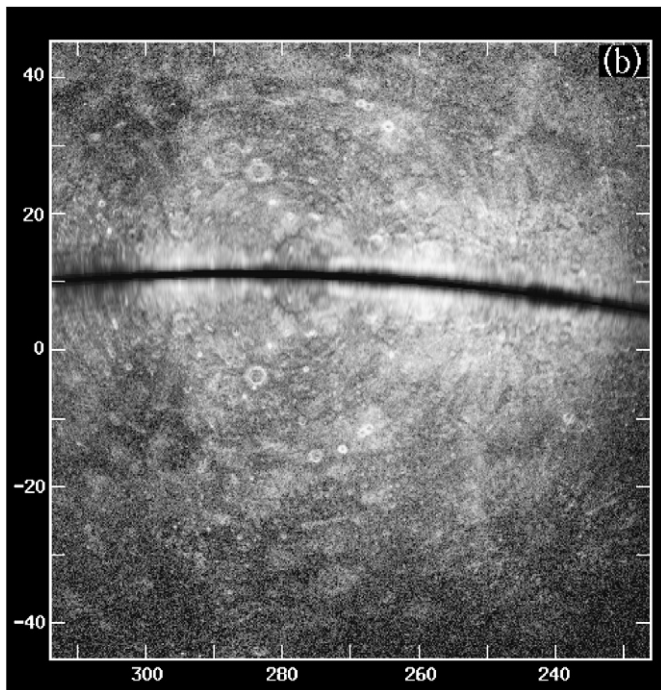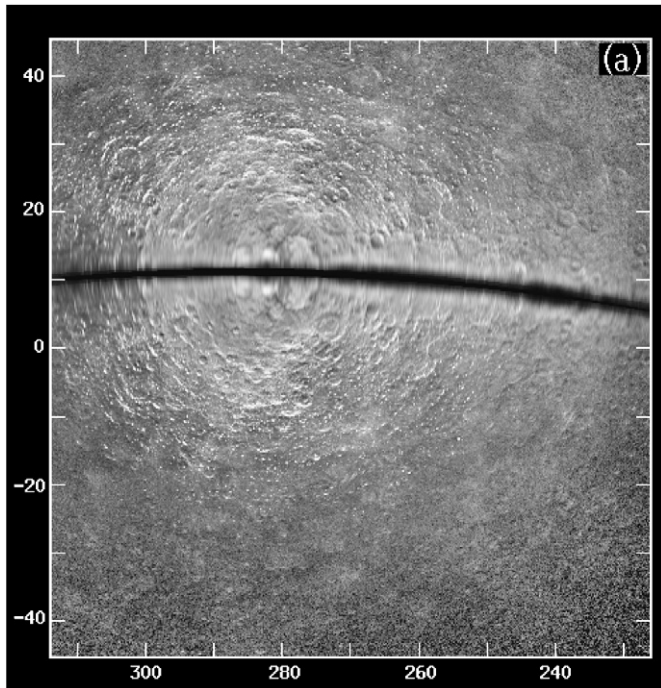
Fig. 38. Arecibo radar images of the "central MUH" region in (a) OC and (b) SC polarizations. The data are from August 14–15, 2004. The gray scale of the SC image has been truncated at 0.5 of the maximum brightness. $\sigma_{\text{sc}}^{\circ}(\text{max.}) = 0.0848$.

Fig. 39. Arecibo radar images of a rayed crater (327° W, 8° N) in (a) OC and (b) SC polarizations. The data are from March 24–25, 2005. $\sigma_{\text{sc}}^{\circ}(\text{max.}) = 0.0670$.

306° W, 20° N (Fig. 36b) also shows up in a VLA image (Fig. 5) and on the VLA contour map (Fig. 4). The brightest of these craters (306° W, 18° N) shows a single ray extending to the ENE in Fig. 36b. Curiously, the brightest spot seen in the Mt. Wilson telescopic images (Dantowitz et al., 2000; Baumgardner et al., 2000), centered near 300° W, 35° N, does not show up prominently in radar images. The closest Arecibo

feature to this is a small bright OC glint with surrounding dark halo at 296° W, 36.5° N (Fig. 36a).

3.5.2. Basins, highlands, and albedo features

Some larger-scale morphological and albedo features can also be seen in the Arecibo images of this region. The OC images (Figs. 36a–38a) reveal a two-ring basin centered at 303° W, 28° N. With inner and outer ring diameters of 156

and 310 km, this basin rivals Homer as the largest two-ring basin on the planet. Interestingly, this basin was actually discovered in 1980 (B.A. Burns and D.B. Campbell, unpublished data) in what was to be one of the only radar interferometric imaging observations of Mercury ever attempted at Arecibo. The SC images (Figs. 36b–38b) show the basin interior to be radar-dark. This is, in fact, part of a larger, very prominent, radar-dark patch that extends on north of the basin. This also shows up as a prominent dark patch in the optical telescopic images (Baumgardner et al., 2000; Mendillo et al., 2001).

Southwest of the two-ring basin is a bright SC patch (Fig. 36b) that starts at the equator near 285° W and runs diagonally northwest to about 298° W, 15° N. (A comparison with Fig. 37b shows that most of this feature lies north of the equator.) To the west of the feature is a triangular dark region that has a narrow connection with the dark patch to the north (containing the two-ring basin) at about 300° W, 20° N. The triangular dark patch is fairly heavily cratered, especially along its eastern edge. The old Arecibo altimetry (Harmon et al., 1986; Harmon and Campbell, 1988) shows that this dark region sits on an isolated 2.5-km-high plateau that runs from about 300° to 312° W at 10° N. This region is also dark in optical telescopic images (Baumgardner et al., 2000; Mendillo et al., 2001; Warell and Limaye, 2001), and the association of this low-albedo region with the plateau was noted by Warell and Limaye. In fact, there appears to be a close correspondence between SC radar albedo and optical telescopic albedo over this entire region. The diagonal bright patch shows up clearly in the Mt. Wilson images, as do the three surrounding dark spots (Baumgardner et al., 2000; Mendillo et al., 2001). Mendillo et al. numbered these dark spots as: "2" for the northern patch including the two-ring basin, "3" for the dark region east of the diagonal patch, and "4" for the dark region on the plateau.

The low region east of the plateau has a smooth, craterless appearance suggestive of smooth plains, as is best seen from the OC image taken on August 14–15, 2004 (Fig. 38a). A portion of this region, from 285° to 298° W at 10° N, also showed smooth, flat topography in the Arecibo altimetry (Harmon et al., 1986; Harmon and Campbell, 1988). Recently, Ksanfomality (2004) has presented evidence for a large circular basin centered at 280° W, 8° N, based on optical telescopic imaging from Skinakas Observatory in Crete (see also Ksanfomality et al., 2005). This basin, informally named "Skinakas Basin" by Ksanfomality, is a two-ring structure with an inner rim diameter of 1000 km. The OC image in Fig. 38a does show some highlighting on the western side of the circular smooth region that may be specular glinting off the inner western basin rim. The SC image in Fig. 36b indicates that the depolarized albedo over the basin floor is nonuniform, with some dark terrain in the center and bright patches in the southwest (the "diagonal patch") and northeast quadrants.

A circular feature (250 km diameter) can be seen on the Doppler equator at 278° W in Fig. 38. This location places it within Skinakas Basin, just east of basin center. The floor is bright in SC, moderately dark in OC, and shows a narrow dark rim-ring in both polarizations. This feature coincides precisely

with a 2.5-km-deep crater feature in the old Arecibo altimetry (Harmon et al., 1986; Harmon and Campbell, 1988). Given its size, it is possible that this is a two-ring basin, and there is a hint of this in both the imagery and altimetry. Just to the southeast of this feature is a smaller two-ring basin centered at 273° W, 3° N. Another two-ring basin of similar size can be seen at 315° W, 18° S in Fig. 36a.

4. Summary and discussion

The major findings from the Arecibo radar imaging of Mercury can be summarized as follows:

(1) Depolarized radar brightness, an indicator of small-scale roughness, is dominated by features associated with fresh impact craters.

(2) The three most prominent radar features seen in the VLA images (all located in the MUH and labelled "A," "B," and "C") can be traced to source craters of diameter 85, 95, and 125 km. Feature "A" is a candidate for the most spectacular radar-rayed crater in the Solar System.

(3) Some "ghost" features are seen which appear similar to "A" but are much fainter, possibly indicating rayed craters caught in an intermediate stage of degradation.

(4) Virtually all optical-rayed craters in the Mariner 10 images show bright depolarized radar features. However, only a small fraction of these show radar rays or other extended radar-bright ejecta.

(5) The most common form for radar-bright craters, especially the smaller ones, is a bright depolarized ring that extends from the inner rim wall to about one crater radius or less beyond the rim. Crater floors tend to be darker, by contrast, although some craters do show a bright floor instead of, or in addition to, a bright rim.

(6) All of the small (unresolved) bright spots in the VLA images have been resolved as bright rim-ring craters in the Arecibo images. Some small, simple (non-ring) bright spots in the Arecibo images are associated with similar bright spots in the Mariner 10 images for which there is no obvious source crater (or for which the crater is lost in the optical glare).

(7) Several craters of various sizes have been seen which show radar-dark haloes.

(8) Craters show a strong correlation between depolarized radar brightness and optical freshness as indicated by their c-class designations in the USGS geologic maps. However, there is a wide range of variation in the radar brightness and morphology of c_5-class craters, with some c_5 craters showing very little radar enhancement. Also, some c_3 and c_4 craters are radar-bright.

(9) The spatial distribution of radar-bright craters appears noticeably non-random at both large and medium scales. For example, the H-7 quadrangle shows an especially high concentration of small bright craters. Also, there are several examples of smaller loose clusterings of small bright craters; these tend to be located in the smoother plains areas.

(10) Large diffuse enhancements in depolarized radar brightness have been found in the circum-Caloris smooth plains (Tir, Budh, and Sobkou Planitiae) and Tolstoj Basin. Some mapped smooth plains in medium-size craters are also radar-bright.

(11) Caloris Basin shows no prominent radar signature, and the interior plains lack the enhanced depolarized brightness of the circum-Caloris smooth plains.

(12) Supporting evidence is found for the large basin-like feature found in telescope imagery of the MUH and centered just north of the equator near 280° W. Several smaller two-ring basins have also been found in the MUH.

Probably the most notable aspect of Mercury's radar appearance is the prominence and variety of fresh impact features. This is something that Mercury shares with the Moon, although there are important differences. Feature "A," that "freshest" of mercurian features, and the similar but fainter "ghost" features, have no true lunar counterparts. Radar ray systems made up of dense collections of narrow rays are not typical of the Moon. Rather, the most prominent radar-rayed crater on the Moon, Tycho, has only a few rays, and these are much longer than mercurian radar rays (Zisk et al., 1974). Gault et al. (1975) argued that the relative compactness of crater ejecta and high density of secondary cratering on Mercury, when compared with the Moon, are a consequence of the larger planet's stronger gravity. Hence, the higher gravity may also explain the density and complexity of fresh radar ray structures on Mercury and the fact that no very long, Tycho-like, radar rays are seen. Another contributing factor to the Mercury/Moon differences may be the possibly higher impact velocities associated with Mercury's location deep in the Sun's potential well (Schultz, 1988). Also, Tycho's long radar rays were observed at X band ($\lambda 3.8$ cm) and, hence, would presumably be associated with finer debris (with longer ballistic trajectories) than that producing S-band rays.

The Mercury/Moon differences may also extend to smaller fresh craters. The most common form for small radar-bright craters on Mercury is a bright rim-ring surrounding a darker floor. Similar bright radar rings have also been seen on the Moon (Zisk et al., 1974; Thompson et al., 1981, 1986) and Venus (Campbell and Burns, 1980). However, bright rings are less common on the Moon than on Mercury, while a higher percentage of fresh lunar craters show bright floors. Furthermore, small to medium-size fresh lunar craters often show bright haloes extending 10–20 crater radii (Thompson et al., 1981), whereas such extended haloes are uncommon on Mercury. The reason for these differences is not obvious, although gravity may again play a role. Gault et al. (1975) have noted a greater degree of post-cratering rim collapse on Mercury than on the Moon, which they attribute to the higher gravity, and it is possible that such post-impact resurfacing may darken initially bright crater floors. Higher gravity may also reduce the incidence of bright haloes on Mercury, although it should be pointed out that the lunar haloes were observed at a shorter wavelength (3.8 cm) and thus may represent backscatter off finer ejecta deposited farther from the source crater than would

be the case at S band (13 cm). Finally, differences in crater maturation rates may affect the appearance of fresh craters. Schultz (1988) has argued that fresh crater degradation from impact gardening proceeds faster on Mercury than on the Moon, so it is possible that this faster degradation could rapidly darken the floors of fresh mercurian craters and obliterate any extended haloes. In their study of bright rim rings on the Moon, Thompson et al. (1986) argued that the flat floors of fresh craters may initially be rough and radar-bright, but then darken as impact gardening smooths the surface; the rims may remain rough and bright for a longer time ". . . owing to preferential downslope movement of fines and continual exposure of fresh blocks." If this same process proceeds more quickly on Mercury, then fresh craters would evolve to the bright-ring stage more rapidly and bright-floored craters would be less common. Different crater degradation rates would also be consistent with the observation of Campbell et al. (1992) that there is a one-to-one correspondence between the presence of optical and radar rays for lunar craters, whereas small optically rayed mercurian craters often do not show radar rays.

It is clear that, to a large extent, the radar appearance of fresh mercurian craters is governed by crater size. The most prominent radar-bright features ("A," "B," "C") and those with the most complex ray systems ("A," and those "ghost" features that appear to be fainter versions of "A") are associated with large craters in the 80–140 km diameter range. Medium-size radar features showing extended ejecta and rays (e.g., Kuiper, Bashō, Degas, MRC-6) are associated with medium-size craters in the 45–70 km diameter range. Still smaller fresh craters, with diameters less than 40 km, tend to show radar-bright rim rings but no radar rays (or at most a single faint ray, as in the case of MRC-7). We have resolved such rim-ring features for craters down to 5-km diameter. Simple (non-ring) bright spots have also been seen which, in some cases, correlate with bright spots in the Mariner images. These may be truly craterless features, or small craters as yet unresolved or whose relief is obscured by their brightness, or extremely fresh, bright-floored craters that have not yet evolved to a bright-ring form. Determining the nature of these bright spots will probably require new spacecraft imagery with higher resolution.

The apparent size-dependence of radar-bright crater morphology may have several causes. As noted by Thompson et al. (1981) in the context of bright-halo lunar craters, the radar signature "is influenced by two major factors: the state of ejecta when it is originally emplaced and its subsequent gardening by meteoroidic bombardment." It is easy to see how large impacts would produce the most extensive radar ray systems, as these high-energy events are the more likely to produce extended blocky ejecta as well as the secondary cratering shown to be associated with some of the radar-bright lunar rays (Pieters et al., 1985). The lack of radar rays from smaller optically rayed craters is understandable when one considers the fundamental differences between optical and radar rays. Optical ray material is believed to be either compositionally different from or more immature than the surface upon which it is emplaced (Pieters et al., 1985; Grier et al., 2001; Hawke et al., 2004). Radar rays, on the other hand, are thought

to be primarily structural, that is, associated with enhanced diffuse/depolarized backscatter off of wavelength-scale surface (or near-surface) roughness elements (Thompson et al., 1981; Pieters et al., 1985). Composition is assumed to play only a secondary role in most radar backscatter, as compositional differences tend to produce less dielectric contrast at radio wavelengths than in the optical. Furthermore, thin surface coatings can strongly affect the optical albedo but be essentially invisible to radar (which responds to dielectric conditions over the full radio skin depth of several meters). It would not be surprising, then, if the smaller fresh impacts were to produce sprays of fine material that show up as optical rays, but lack the energy to throw out boulder-size ejecta (or produce secondary craters) at comparable distances from the primary crater. Alternatively, it is possible that some of the smaller optical-rayed mercurian craters are born with radar rays, but that these structural rays are destroyed by impact gardening at a faster rate than for the optical rays and also at a faster rate than for radar rays from larger impacts. Thompson et al. (1981) have, in fact, suggested that radar-bright crater structures on the Moon have a shorter lifetime for smaller craters than for larger ones, which seems plausible if the ejecta deposits from the smaller impacts are thinner or if smaller blocks are broken down faster. A similar effect has been noted for the size dependence of the maturation time for the optical brightness of lunar craters (Grier et al., 2001).

Crater-size-dependent effects aside, there is ample evidence that, in general, crater maturation on Mercury advances much more rapidly for radar brightness than for optical brightness. Nothing demonstrates this better than the wide variation in radar brightness amongst c_5-class craters. Crater Bartok, for example, is a bright c_5 crater optically, but appears as a degraded "ghost" crater in the radar images. There are other c_5-class craters such as Tyagaraja that show almost no enhanced radar brightness, while the nearby c_5 crater Balzac shows a very bright rim ring. Finally, there is the near-absence of radar rays from the smaller optical-rayed craters in Table 2 (nearly all of which are c_5 class). In conclusion, it appears that a significant fraction of the radar maturation time scale is contained within the c_5-class age span. It should not be forgotten, however, that we have found a number of c_3- and c_4-class craters showing high radar brightness. Presumably these craters have managed to maintain a small-scale freshness despite showing a more degraded appearance in the Mariner images.

Finally, on the subject of crater radar morphology, there is the interesting case of the dark-halo craters. These resemble dark-halo craters seen in radar images of the Moon (Ghent et al., 2005). Like their lunar counterparts, the mercurian dark-halo craters are not especially common. The lunar dark haloes have been attributed to burial by a homogeneous ejecta blanket devoid of radar scatterers, and a similar explanation may apply to the mercurian craters.

In Section 3 we pointed out several instances of apparent clustering of radar-fresh craters. Perhaps the most important example of this is the relative abundance of radar-bright craters in the H-7 quadrangle, which suggests that the similar abundance of optically bright craters in the Mariner images of the region was not simply an artifact of the high Sun angles during the flybys. Smaller-scale clusterings were also noted in the circum-Caloris smooth plains, in an "intermediate plains" region in the H-2 quadrangle, and just NE of feature "C." The likelihood that at least some of these clusterings are located in smooth plains or other putative lava flows suggests the possibility that the crater maturation process is somehow retarded in such flows or that these surfaces are more conducive to the production of blocky ejecta. This may not explain the abundance of bright craters over H-7, nor should the possibility of a non-random spatial distribution of impacts be dismissed. It should be noted that fresh crater clusterings have also been seen in radar observations of Venus (Campbell and Burns, 1980).

Among the more interesting and unexpected findings from Mercury radar imagery is the enhanced depolarized brightness observed from the smooth plains. Just the reverse radar albedo contrast is seen for the Moon, where the lunar maria appear radar-dark relative to the highlands (Zisk et al., 1974; Thompson, 1987; Campbell et al., 1997). It has been argued that the radar darkness of the lunar maria can be attributed to a relatively high iron and titanium content that increases the electrical lossiness of the mare lavas and inhibits volume scattering from subsurface roughness (Campbell et al., 1997). The mercurian surface, on the other hand, shows a generally low microwave opacity (Mitchell and de Pater, 1994) indicative of a highly differentiated, possibly non-basaltic crust that is relatively transparent to radio waves (Jeanloz et al., 1995). Although the mercurian smooth plains may well be lava flows (Strom, 1979), the suggestion is that these lavas are compositionally different from, and less electrically lossy than, mare lavas. However, this does not necessarily explain why the smooth plains have higher SC radar brightness than the adjacent intercrater plains. Robinson and Lucey (1997) found some color variations in Mariner images of H-6 that are suggestive of variations in iron content, with some of the bluer (less ferric) regions possibly being lava flows. On the other hand, there is no obvious indication from the microwave emissivity images that the microwave opacity of the circum-Caloris region is much different from the global average (Mitchell and de Pater, 1994; Jeanloz et al., 1995). Of course, greater transparency to volume scattering may not be the only determinant of SC brightness. It is also possible that the smooth plains may have rougher small-scale surface texture that may or may not be related to volcanic rheology. If volcanic, the smooth plains SC brightness might be a weaker version of the high depolarized brightness seen from the younger martian lava flows (Harmon et al., 1999). Also, given that the smooth plains are younger than the intercrater plains, any surface or near-surface roughness may be less degraded by impact gardening than are the older intercrater plains (in an analogous sense to the maturation of crater ejecta). Finally, it is possible that the smooth plains brightness is due to a higher dielectric constant.

Radar-bright "smooth plains" (that is, terrain designated "ps" in the USGS geologic maps) are not restricted to the circum-Caloris planitiae such as Tir and Budh, but are also found in some older, degraded impact structures such as Tolstoj Basin and some medium-size craters in the H-7 quadrangle. The radar

brightness of the Tolstoj plains suggests that they may be a similar (volcanic?) material to that filling the circum-Caloris planitiae, and possibly of a similar age. The SC radar brightness certainly supports the conclusion by Spudis and Guest (1988) that "the interior of Tolstoj is flooded with smooth plains that clearly postdate the basin deposits." The same might also be said of the other degraded craters with radar-bright floors.

While it is possible that the smooth plains brightness is associated with extrusive volcanism, our imaging reveals no evidence of volcanic constructs as such. Feature "B," the one MUH feature considered a candidate volcano based on the pre-upgrade Arecibo images, now appears to be an impact crater, and our post-upgrade images show no other obvious volcano candidates in the MUH.

5. Concluding remarks

The main objective of this paper has been to present an overview of radar imaging results for Mercury based on observations with the upgraded Arecibo telescope. Although we have offered some evaluation of our findings, this has been largely preliminary and qualitative. More detailed and quantitative work is planned which will include, for example, a compilation of crater statistics and a more detailed study of radar polarization characteristics (including measurement of polarization ratios and a search for linearly polarized echoes indicative of subsurface scattering). Nevertheless, the results presented here should serve as a preview of some of the regions warranting a closer look by the upcoming spacecraft missions to the planet, as well as a useful database for making further radar/optical comparisons when the images anticipated from those missions become available.

Acknowledgments

References

Baumgardner, J., Mendillo, M., Wilson, J.K., 2000. A digital high-definition imaging system for spectral studies of extended planetary atmospheres. I. Initial results in white light showing features on the hemisphere of Mercury unimaged by Mariner 10. Astron. J. 119, 2458–2464.

Butler, B.J., 1994. 3.5-cm radar investigation of Mars and Mercury: Planetological implications. Ph.D. thesis. California Institute of Technology, Pasadena.

Butler, B.J., Muhleman, D.O., Slade, M.A., 1993. Mercury: Full-disk radar images and the detection and stability of ice at the north pole. J. Geophys. Res. 98, 15003–15023.

Campbell, D.B., Burns, B.A., 1980. Earth-based radar imagery of Venus. J. Geophys. Res. 85, 8271–8281.

Campbell, B.A., Bell, J.F., Zisk, S.H., Hawke, B.R., Horton, K.A., 1992. A high-resolution radar and CCD imaging study of crater rays in Mare Serenitatis and Mare Nectaris. Proc. Lunar Sci. Conf. 22, 259–274.

Campbell, B.A., Hawke, B.R., Thompson, T.W., 1997. Regolith composition and structure in the lunar maria: Results of long-wavelength radar studies. J. Geophys. Res. 102, 19307–19320.

Clark, P.E., Leake, M.A., Jurgens, R.F., 1988. Goldstone radar observations of Mercury. In: Vilas, F., Chapman, C.R., Matthews, M.S. (Eds.), Mercury. Univ. of Arizona Press, Tucson, pp. 77–100.

Dantowitz, R.F., Teare, S.W., Kozubal, M.J., 2000. Ground-based high-resolution imaging of Mercury. Astron. J. 119, 2455–2457.

Davies, M.E., Dwornik, S.E., Gault, D.E., Strom, R.G., 1978. Atlas of Mercury. NASA, Washington, DC.

De Hon, R.A., Scott, D.H., Underwood, J.R., 1981. Geologic map of the Kuiper (H-6) quadrangle of Mercury. USGS Map I-1233, U.S. Geol. Surv., Denver, CO.

Gault, D.E., Guest, J.E., Murray, J.B., Dzurisin, D., Malin, M.C., 1975. Some comparisons of impact craters on Mercury and the Moon. J. Geophys. Res. 80, 2444–2460.

Ghent, R.R., Leverington, D.W., Campbell, B.A., Hawke, B.R., Campbell, D.B., 2005. Earth-based observations of radar-dark crater haloes on the Moon: Implications for regolith properties. J. Geophys. Res. 110, doi:10.1029/2004JE002366.

Goldstein, R.M., 1970. Mercury: Surface features observed during radar studies. Science 168, 467–468.

Goldstein, R.M., 1971. Radar observations of Mercury. Astron. J. 76, 1152–1154.

Grier, J.A., McEwen, A.S., Lucey, P.G., Milazzo, M., Strom, R.G., 2001. Optical maturity of ejecta from large rayed lunar craters. J. Geophys. Res. 106, 32847–32862.

Guest, J.E., Greeley, R., 1983. Geologic map of the Shakespeare (H-3) quadrangle of Mercury. USGS Map I-1408, U.S. Geol. Surv., Denver, CO.

Hapke, B., Danielson, G.E., Klaasen, K., Wilson, L., 1975. Photometric observations of Mercury from Mariner 10. J. Geophys. Res. 80, 2431–2443.

Harmon, J.K., 1997. Mercury radar studies and lunar comparisons. Adv. Space Res. 19 (10), 1487–1496.

Harmon, J.K., 2002. Planetary delay-Doppler radar and the long-code method. IEEE Trans. Geosci. Remote Sensing 40, 1904–1916.

Harmon, J.K., Campbell, D.B., 1988. Radar observations of Mercury. In: Vilas, F., Chapman, C.R., Matthews, M.S. (Eds.), Mercury. Univ. of Arizona Press, Tucson, pp. 101–117.

Harmon, J.K., Slade, M.A., 1992. Radar mapping of Mercury: Full-disk images and polar anomalies. Science 258, 640–643.

Harmon, J.K., Campbell, D.B., Bindschadler, D.L., Head, J.W., Shapiro, I.I., 1986. Radar altimetry of Mercury: A preliminary analysis. J. Geophys. Res. 91, 385–401.

Harmon, J.K., Slade, M.A., Vélez, R.A., Crespo, A., Dryer, M.J., Johnson, J.M., 1994. Radar mapping of Mercury's polar anomalies. Nature 369, 213–215.

Harmon, J.K., Arvidson, R.E., Guinness, E.A., Campbell, B.A., Slade, M.A., 1999. Mars mapping with delay-Doppler radar. J. Geophys. Res. 104, 14065–14090.

Harmon, J.K., Perillat, P.J., Slade, M.A., 2001. High-resolution radar imaging of Mercury's north pole. Icarus 149, 1–15.

Hawke, B.R., Head, J.W., 1977. Impact melt on lunar crater rims. In: Roddy, D.J., Pepin, R.O., Merrill, R.B. (Eds.), Impact and Explosion Cratering. Pergamon Press, New York, pp. 815–841.

Hawke, B.R., Blewett, D.T., Lucey, P.G., Smith, G.A., Bell, J.F., Campbell, B.A., Robinson, M.S., 2004. The origin of lunar crater rays. Icarus 170, 1–16.

Herrick, R.R., Forsberg-Taylor, N.K., 2003. The shape and appearance of craters formed by oblique impact on the Moon and Venus. Meteorit. Planet. Sci. 38, 1551–1578.

Jeanloz, R., Mitchell, D.L., Sprague, A.L., de Pater, I., 1995. Evidence for a basalt-free surface on Mercury and implications for internal heat. Science 268, 1455–1457.

King, J.S., Scott, D.H., 1990. Geologic map of the Beethoven (H-7) quadrangle of Mercury. USGS Map I-2048, U.S. Geol. Surv., Denver, CO.

Ksanfomality, L.V., 2004. A huge basin in the unknown portion of Mercury in the 250°–290° W longitude range. Solar System Res. 38, 21–27.

Ksanfomality, L., Papamastorakis, G., Thomas, N., 2005. The planet Mercury: Synthesis of resolved images of unknown part in the longitude range 250°–290° W. Planet. Space Sci. 53, 849–859.

McGill, G.E., King, E.A., 1983. Geologic map of the Victoria (H-2) quadrangle of Mercury. USGS Map I-1409, U.S. Geol. Surv., Denver, CO.

Mendillo, M., Warell, J., Limaye, S.S., Baumgardner, J., Sprague, A., Wilson, J.K., 2001. Imaging the surface of Mercury using ground-based telescopes. Planet. Space Sci. 49, 1501–1505.

Mitchell, D.L., de Pater, I., 1994. Microwave imaging of Mercury's thermal emission at wavelengths from 0.3 to 20.5 cm. Icarus 110, 2–32.

Muhleman, D.O., Butler, B.J., Grossman, A.W., Slade, M.A., 1991. Radar images of Mars. Science 253, 1508–1513.

Muhleman, D.O., Grossman, A.W., Butler, B.J., 1995. Radar investigation of Mars, Mercury, and Titan. Annu. Rev. Earth Planet. Sci. 23, 337–374.

Pieters, C.M., Adams, J.B., Mouginis-Mark, P.J., Zisk, S.H., Smith, M.O., Head, J.W., McCord, T.B., 1985. The nature of crater rays: The Copernicus example. J. Geophys. Res. 90, 12393–12413.

Pike, R.J., 1988. Geomorphology of impact craters on Mercury. In: Vilas, F., Chapman, C.R., Matthews, M.S. (Eds.), Mercury. Univ. of Arizona Press, Tucson, pp. 165–273.

Robinson, M.S., Lucey, P.G., 1997. Recalibrated Mariner 10 color mosaics: Implications for mercurian volcanism. Science 275, 197–200.

Schaber, G.G., McCauley, J.F., 1980. Geologic map of the Victoria (H-8) quadrangle of Mercury. USGS Map I-1199, U.S. Geol. Surv., Denver, CO.

Schultz, P.H., 1988. Cratering on Mercury: A relook. In: Vilas, F., Chapman, C.R., Matthews, M.S. (Eds.), Mercury. Univ. of Arizona Press, Tucson, pp. 274–335.

Slade, M.A., Butler, B.J., Muhleman, D.O., 1992. Mercury radar imaging: Evidence for polar ice. Science 258, 635–640.

Spudis, P.D., Guest, J.E., 1988. Stratigraphy and geologic history of Mercury. In: Vilas, F., Chapman, C.R., Matthews, M.S. (Eds.), Mercury. Univ. of Arizona Press, Tucson, pp. 118–164.

Spudis, P.D., Prosser, J.G., 1984. Geologic map of the Michelangelo (H-12) quadrangle of Mercury. USGS Map I-1659, U.S. Geol. Surv., Denver, CO.

Strom, R.G., 1979. Mercury: A post-Mariner 10 assessment. Space Sci. Rev. 24, 3–70.

Thomas, P.G., 1997. Are there other tectonics than tidal despinning, global contraction and Caloris related events on Mercury? A review of questions and problems. Planet. Space Sci. 45, 3–13.

Thompson, T.W., 1987. High-resolution lunar radar map at 70-cm wavelength. Earth Moon Planets 37, 59–70.

Thompson, T.W., Zisk, S.H., Shorthill, R.W., Schultz, P.H., Cutts, J.A., 1981. Lunar craters with radar bright ejecta. Icarus 46, 201–225.

Thompson, T.W., Saunders, R.S., Weissman, D.E., 1986. Lunar and venusian radar bright rings. Earth Moon Planets 36, 167–185.

Trask, N.J., Dzurisin, D., 1984. Geologic map of the Discovery (H-11) quadrangle of Mercury. USGS Map I-1658, U.S. Geol. Surv., Denver, CO.

Warell, J., Limaye, S.S., 2001. Properties of the Hermean regolith: Global regolith albedo variation at 200 km scale from multicolor CCD imaging. Planet. Space Sci. 49, 1531–1552.

Zisk, S.H., Pettengill, G.H., Catuna, G.W., 1974. High-resolution radar map of the lunar surface at 3.8-cm wavelength. Moon 10, 17–50.

Zohar, S., Goldstein, R.M., 1974. Surface features on Mercury. Astron. J. 79, 85–91.